Collective fate decisions and cell rearrangements underlie gastruloid symmetry breaking

David Oriola[1,2,*], Gabriel Torregrosa-Cortés[3,*], Sotiris Samatas[1,2], Krisztina Arató[1], David Fernández-Munuera[1], Elisa Maria Hahn[1], Kerim Anlaş[1], Jordi Garcia-Ojalvo[2,3] & Vikas Trivedi[1,2,4]

[1]EMBL Barcelona, Barcelona Biomedical Research Park, 08003, Barcelona, Spain
[2]Barcelona Collaboratorium for Modelling and Predictive Biology, 08005 Barcelona, Spain
[3]Department of Medicine and Life Sciences, Universitat Pompeu Fabra, Barcelona Biomedical Research Park, 08003 Barcelona, Spain
[4]EMBL Heidelberg, Developmental Biology Unit, 69117 Heidelberg, Germany
[*]These authors contributed equally to this work

How cell fate decisions coordinate with tissue-scale morphogenesis remains a major challenge in developmental biology. Gastruloids, three-dimensional aggregates of pluripotent stem cells that self-organise and break symmetry via polarised Brachyury/T expression, provide an ideal system to address this question. By generating gastruloids with defined initial proportions of T-expressing cells, we show that fate decisions occur collectively, with the pluripotent population delaying differentiation and controlling the timing of symmetry breaking. Mechanical measurements reveal differences in surface tension between T-positive and T-negative tissues, consistent with radial cell sorting. Finally, incorporating fate dynamics and mechanics into a computational model recapitulates the sequential symmetry-breaking events observed in vitro. Our findings identify a mechanochemical mechanism underlying axis formation, and demonstrate how multicellular systems can robustly self-organise without external signalling cues.

Introduction

How animals establish the body plan is a fundamental problem in biology (*1, 2*). Molecular cues from extra-embryonic tissues polarise the early embryo thus generating a coordinate system for subsequent regional patterning (*3–7*). In the last decade, several studies have shown that collections of stem cells can break symmetry *in vitro* even in the absence of instructive signals (*8–12*). Gastruloids (*10, 13–16*) are three-dimensional aggregates of pluripotent stem cells that self-organise and break symmetry via polarised Brachyury/T expression (*17*), providing an ideal system to study spontaneous formation of the primary body axis *in vitro*. Recent studies suggest that cell rearrangements are the main driving mechanism of symmetry breaking in this system (*18–20*). At the same time, gene expression patterns have been shown to scale with system size, with larger gastruloids showing delayed symmetry breaking (*21–23*), suggesting a tight coordination between morphogenetic movements and cell fate transitions. How the interplay between these two processes drives symmetry breaking in this system remains elusive.

Here we address this question by combining cell proportion experiments with single-cell RNA sequencing, biophysical measurements, and computational modelling. By systematically varying the initial fraction of Brachyury/T-expressing cells (T+ cells), we show that the timing of symmetry breaking and subsequent gastruloid elongation depends on the initial T+ population. Mathematical modelling further reveals that cell differentiation in gastruloids is non-cell autonomous, with fate decisions emerging at the collective level. This is accompanied by a radial organisation of cell fates prior to polarisation, with T- cells preferentially localising to the aggregate periphery and T+ cells being in the core. These spatial differences correlate with surface tension variations between T+ and T- tissues, consistent with a radial cell sorting process. Finally, integrating fate dynamics and mechanics *in silico* recapitulates the stages of symmetry

breaking observed experimentally. Together, our results provide a mechanochemical framework for self-organisation in 3D embryo-like structures and establish a systematic approach to dissect cellular feedbacks *in vitro*.

Results

T population dynamics is dependent on the initial fraction of T+ cells in gastruloids

The ability of gastruloids to polarise and elongate is known to be dependent on the initial conditions, such as stem cell pluripotency, culture media composition or initial aggregate size (*24–27*). For example, initial heterogeneity on the levels of T or Wnt signalling are known to increase the variability in gastruloid formation (*10, 19, 25, 28, 29*). Motivated by the previous studies, we asked whether the initial state of the cells could serve as a proxy for the timing of symmetry breaking and elongation in gastruloids. To address this, we systematically varied the proportion of T+ cells at the time of seeding, following a strategy similar to the one used in chimeric embryo experiments (*30*). The canonical gastruloid protocol consists on the aggregation of ~ 300 mouse embryonic stem cells (mESC) followed by CHIR-99021 (CHIR) treatment betwen 48-72 hours post aggregation (hpa) (*10, 13, 31*). Gastruloids polarise around 72 hpa and rapidly elongate at 96 hpa. We decided to follow the same protocol but growing gastruloids in the absence of a CHIR pulse (*32, 33*) to study the inherent signalling dynamics of cells. We used an E14 Bra/T::GFP cell line to visualise T expression and cells were maintained in ES-Lif (ESLIF) medium. In these conditions, typically $\lesssim 5\%$ of cells differentiate to become T+ (see Materials and Methods). We took advantage of this fact to sort T+ and T- cells from culture via fluorescence-activated cell sorting (FACS) and generate 3D aggregates with controlled T+ fractions. T+ and T- cells were mixed in different proportions to form 3D cell aggregates in ultra-low adherence multiwell plates (Fig. 1A). By using the GFP signal as a proxy for the T+

cell population, we estimated the fraction of T+ cells over time, $\phi(t)$ (Fig. 1B,C,D, Fig. S1A and Materials and Methods). While tissue polarisation was observed in all cases, the time of polarisation varied depending on the initial T+ fraction (Fig. 1C and Fig. S1C). The change in T dynamics depending on the inital T+ fraction became more evident when the average fraction of T+ cells (ϕ) was plotted as a function of the initial T+ fraction ($\phi(0)$) at 24, 48 and 72 hpa (Fig. 1D). Cell aggregates that were initially formed with a large amount of T+ cells ($\phi(0) \gtrsim 0.5$) polarised and elongated at 48 hpa instead of at 72 hpa (Fig. 1B,C and Fig. S1B,C). The fact that a high T+ population favors rapid polarisation is analogous to the high expression of T+ cells following the addition of CHIR in the canonical protocol, which leads to fast polarisation and elongation (*10, 13*). Notably, the timing and degree of elongation were also affected depending on the initial T+ fraction (Fig. 1E and Fig. S1B). We thus conclude that, while gastruloids can polarise and elongate irrespective of the initial fraction of T+ cells, the timing of symmetry breaking and elongation is dependent on the initial T+ fraction.

Single-cell RNA-seq allows the identification of the major cellular states during early gastruloid differentiation

The cellular identity of T- cells in our experiments is compatible with both a pluripotent state as well as with a differentiated mesoderm state in which T expression was lost. In order to discern between these two cases and to allow for the identification of the major cellular states, we made use of our previously published single-cell RNA sequencing dataset (*32*). We focused on the cell fate dynamics from 24-48 hpa by integrating both time points (Fig. 2A, gray data points in the background). Given the challenges of classical clustering and annotation approaches to split states with subtle gene modifications, we decided to use a custom annotation approach (see Materials and Methods) using cell fate markers known in the literature. Using this method, we annotated the major cellular fates and their proportions, as well as their time evolution tra-

jectories (Fig. 2A,B, Figs. S2, S3 and Table S1). Compared to other methods which require many annotation markers (*34*), our simple method provides a robust approach more suitable for the annotation of continuous processes with small transcriptomic differences. We further validated the consistency of our annotation approach with traditional clustering methods, showing good agreement between communities discovered and annotation (see Fig. S2B, C, E). At 24 hpa, approximately one-third of the cells were found in an epiblast/pluripotent state (Nanog+, Sox2+) while the remaining two-thirds started transitioning to primitive streak-like states (see Fig. 2A and Fig. S2D). A large population of those differentiated cells ($\simeq 63\%$) were Nanog+, T+, which we may refer to as posterior epiblast-like. The remaining fraction of differentiated cells consisted mainly on a Nanog-, T+ population ($\simeq 31\%$) referred to as a posterior primitive-streak-like state and only a minority of cells ($\simeq 6\%$) were found in anterior mesoderm-like (Eomes+, Gata6+, Mesp1+) or endoderm-like (Eomes+, Gata6+, Sox17+) states (see Fig. 2A). The scenario at 48 hpa showed an increase of the posterior primitive streak-like population (Nanog-, T+) coming from cells differentiating from the posterior epiblast-like state. Finally, the differentiation of Nanog-, T+ cells contributed to the emergence of a posterior mesoderm-like state (Aldh1a2+, Tbx6+) (see Fig. 2A, C, E S2). Overall, the previous results recapitulate an analogous progression of the bifurcation tree observed in the mouse embryo (*35*). A similar analysis on a second replicate experiment resulted in the same conclusions stated above (see Fig. S3).

To verify the progression and the spatial patterning of the previously identified cellular states, we performed RNA hybridization chain reaction (HCR) stainings. Given that experimentally we have access to the dynamics of the T+ state, we broadly classify all cell types into 3 states: Nanog+ pluripotent state (state A, cluster 1), T+ primitive streak-like state (state B, clusters 2 and 3) and further differentiated states Aldh1a2+ and Gata6+ (state C, clusters 4,5

and 6). We stained for markers of these states at 24, 48 and 72 hpa in gastruloids (Fig. 2D and Fig. S4) and on purely T- ($\phi = 0$) and T+ ($\phi = 1$) FACS sorted aggregates (Fig. S5). Nanog was homogeneously distributed at 24 hpa for both control gastruloids and T- sorted aggregates and was found in small clusters in the anterior region at 72 hpa (see Figs. 2D,S4 and S5). Conversely, T+ aggregates showed low Nanog expression at 24 hpa and no expression at 48 hpa, with structures resembling small 72 hpa gastruloids (Fig. S5). We thus conclude that T+ cells (state B) cannot differentiate back to the pluripotent state (Nanog+, state A). Interestingly, we observed that cells in state C (expressing Aldh1a2 and/or Gata6) were restricted to the periphery in both gastruloids (Fig. 2D) and T- sorted aggregates at 48 hpa (Fig. S4, S5). Similarly, Aldh1a2 and Gata6 were preferentially found on the periphery of the 24 hpa T+ aggregates (see Fig. S5). At 72 hpa, Aldh1a2 and Gata6 were found in the anterior region of T- sorted aggregates and gastruloids, consistent with previous work (*13, 32*). Overall, our results show that early signs of radial symmetry breaking on T expression are already present at 48 hpa, prior to proper gastruloid polarisation at 72 hpa.

T- cells are enriched on the periphery of the 3D aggregates in cell proportion experiments

The previous HCR stainings show that state C (T-) cells form clusters on the periphery of 48 hpa gastruloids while state B (T+) cells are found on the core (Fig. 2D). Given recent evidences of cell sorting in gastruloids depending on Wnt activity (*19*), we decided to explore if state A cells (T-) would also be restricted to the periphery of the aggregates in our cell proportion experiments. Given that our cell line had a single cell reporter (Bra::GFP), it was not a priori possible to distinguish A-B from B-C transitions. In order to circumvent this problem, we made use of exogenous labelling of cells with a SiR-DNA dye (see Fig. 3A,B and Fig. S6A). When initially labelling the T- population (A state) with the dye, cells that were SiR-DNA+, T+ af-

ter 24h corresponded to T- cells that activated T (p-transition, see Fig. 3B). Conversely, when initially labelling the T+ population, cells that were SiR-DNA+, T- after 24h would correspond to T+ cells that turned off T (q-transition, see Fig. 3B). To confirm that the SiR-DNA dye was not affecting the cells, we labelled the T+ and T- populations and did not find any effect on T proportions (see Fig. S6B).

We first mixed 50/50 T+ and T- cells and labelled the latter population with SiR-DNA (Fig. 3C). At 24 hpa, we found that the cells that did not activate T (T-, SiR-DNA+) were enriched on the periphery of the aggregates (see Fig. 3C, upper panel). This was further quantified by computing the radial intensity profile of the difference between the normalised SiR-DNA and T signals (Fig. 3C, lower panel; see Materials and Methods). As a control, we mixed SiR-DNA labelled T- and unlabelled T- cells (50/50 ratio) and the enrichment was lost as expected (see Fig. 3C, blue case). Hence, provided that all cells are initially T-, no radial differences in the T population are found during the first 24 hpa. Interestingly, despite radial differences in T expression were found in the 50/50 mixing case, no significant spatial variations in the SiR-DNA signal were detected (Fig. 3C, inset). This result rules out pure cell sorting as the sole mechanism driving the observed spatial pattern of T expression during the first 24 hpa. However, this observation is compatible with a scenario in which cell sorting and fate transitions occur simultaneously. Indeed, if one were to assume that T- cells sort to the periphery and T+ cells sort to the core in the 50/50 mixing case, the flux of labelled T- cells that move from the core to the periphery could be balanced by the flux of labelled T- cells that activate from the periphery and move to the core. Radial differences in T expression were consistently found when mixing T+ and T- cells in different proportions (see Figs. 3D, S6 and S7). In particular, when starting with a purely T+ aggregate and labelled with SiR-DNA half of the cells, after 24h the cells that de-activated (T-, SiR-DNA+) were also enriched in the outer region while T+

cells remained enriched in the core (see Figs. S6A and S7 cases $\phi = 1$). This was consistent with our HCR stainings of purely T+ aggregates at 24 hpa (see Fig. S5). Hence, our results show that T- cells are enriched on the periphery of the aggregates irrespective of their previous T expression history (i.e. both A and C states). We thus conclude that cell sorting and cell fate transitions are likely to occur simultaneously in the aggregates and contribute to the observed spatial differences in T expression. This led us to hypothesise possible differential mechanics between T+ and T- cells leading to mechanical cell sorting.

T+ and T- cell aggregates exhibit differential tissue mechanics

To investigate if the final spatial organisation on T expression was a consequence of differential tissue mechanics, we performed fusion experiments as well as nanoindentation to characterise the tissue mechanical properties (Fig. 4A) (*23, 36, 37*). We found that pairs of T+ cell aggegates fused completely after 10 h while pairs of T- aggregates exhibited a phenomenon known as arrested coalescence, i.e. incomplete fusion (*36*) (Fig. 4A, right and Fig. 4B). Our results align with recent findings where T KO cellular aggregates also exhibited partial fusion as opposed to wildtype aggregates (*23*). Interestingly, the dynamics of heterotypic pairs (T+,T-) was clearly different from the homotypic ones (T+,T+ or T-,T-), hinting to the presence of an interfacial tension between tissue types (Fig. 4B, orange curve). We next decided to explore if 24 hpa and 48 hpa gastruloids have similar mechanical properties compared to T- and T+ aggregates, respectively. To do this, we performed the same set of homotypic fusion experiments using 24 hpa and 48 hpa gastruloids. Indeed, similar trends were observed akin to the T- and T+ homotypic fusions, namely 24 hpa pairs exhibited arrested coalescence while 48 hpa pairs fused completely (see Fig. 4C). This is consistent with the timeline of gastruloid differentiation, where T expression is upregulated around 48 hpa. We next performed nanoindentation measure-

ments of the aggregates to measure the effective tissue elasticity (see Materials and Methods). By combining the estimate parameters from the fusion experiments and the nanoindentation measurements, we could infer the surface tension γ and viscosity η of the aggregates (*36*). We found a $\sim$ 3-fold increase in surface tension γ and a $\sim$2-fold increase in viscosity η for T+ aggregates compared to T- aggregates (see Fig. 4D, E, F). The effective elasticity was found to be slightly lower for T+ aggregates compared to T- aggregates (Fig. 4F). While 48 hpa gastruloids showed a similar 3-fold increase in surface tension with respect to 24 hpa gastruloids, this was not the case for viscosity which remained similar. We reason that this might be a consequence of the fact that 48h gastruloids have a substantial fraction of T- cells ($\sim$ 50 %, see Fig. 1D) that contribute to a lower tissue viscosity. Overall, our results in Fig. 4 are compatible with the classical picture of mechanical cell sorting, where the higher surface tension tissue stays in the core while the lower surface tension tissue is restricted to the periphery (*38, 39*). Well known candidate proteins driving these different tissue affinities are cadherins (*39–41*). Indeed, we confirmed such a difference at the protein level using Western blots (see Fig. S8) and found that N-cadherin (Cdh2) levels were higher in T+ aggregates than in T- aggregates. Conversely, E-cadherin (Cdh1) levels were higher in T- than in T+ aggregates. Similarly, RNA expression of the homologous cadherins showed differential expression between pluripotent and primitive streak-like states, giving additional support to this evidence (see Fig. 2E). We thus conclude that differential cadherin levels might be involved in the sorting process, in line with other studies on gastruloids (*18, 19*). In all, we find changes in the material properties of gastruloids from 24 to 48 hpa which are concomitant with the increase in T+ population during this same time period.

Cell-cell communication explains T proportions in the 3D cellular aggregates

The fact that no spatial variations in the SiR-DNA signal were found in the cell proportion experiments (Fig. 3C, inset) implies that cell sorting is not the only mechanism at play and suggests that cell differentiation also plays an important role during symmetry breaking. We thus asked if cell-cell communication is required to explain T dynamics in the cell proportion experiments in Fig. 1. We first noticed that the non-monotonous behaviour at 48 hpa in Fig. 1D is incompatible with a simple linear stochastic process (*42, 43*) of autonomous cell fate decisions. This is because such a process leads to a linear dependence of the fraction $\phi(t)$ of T+ cells at a time t on the initial fraction $\phi(0)$ (see Appendix). Hence, we argue that some form of cell-cell communication is necessary to account for the nonlinear dependence on the initial cell populations observed in the experiments. We considered a minimal three-state model (*43–46*) consistent with our analysis of scRNA-seq data (Fig. 5A). We performed a numerical exploration of 24 possible cell signalling models in which states A and B can control differentiation through cellular feedback (see Fig. S9 and Appendix) and found that, in the mean field approximation, the models that best fit the data correspond to the ones where the pluripotent population (state A) inhibits cell differentiation, specifically the B-C transition (see Figs. S9, S10). Such a cell-cell signalling scenario has been considered as a plausible paracrine feedback mechanism, whereby residual pluripotent cells inhibit cell differentiation (*43*). In Fig. 5A,B,C (left) and Fig. S1A we show the model that best fits our experimental data, which considers state A inhibiting both p and q-transitions. From the fit we obtain the transition rates ($p = 0.14 \pm 0.01$ h^{-1}, $q = 0.071 \pm 0.003$ h^{-1}, mean $\pm$ SD) as well as the feedback strength parameter ($K = 0.17 \pm 0.02$, mean $\pm$ SD). Hence, a simple three-state model with cell-cell communication accounts for the experimental results.

We next asked how the parameters in our differentiation model are affected under perturbations of Wnt, Fgf and Nodal/Tgf-β, which are known to be the main signalling pathways involved in symmetry breaking (*13, 32, 47, 48*). In all three cases, the model showed that the p-transition was abolished, while the q-transition remained unaffected (Figs. 5, S11,S12 and S13 and Table S3). To verify the results of the model, we considered the case of 50/50 T+/T- starting populations under Fgf inhibition with PDO3. In this case, the model predicted that after 48h, the A-state cells do not transition to state B because of Fgf inhibition, while almost all B cells transition to state C. This was confirmed through HCR stainings where the T (state B) signal was almost absent while Nanog and Aldh1a2, Gata6 signals (states A and C, respectively) were the dominant ones (see Fig. S11). Our results suggest that Wnt, Fgf and Nodal/Tgf-β are required for primitive streak formation (state B) while leaving mesoderm formation (state C) unaffected, in line with recent findings on Wnt and Nodal signalling in gastruloids (*48*).

Finally, our model suggests that Nodal/Tgf-β inhibition abolishes cell-cell communication (see Fig. 5, right) as opposed to the inhibition of Wnt or Fgf signalling (see Figs. S12 and S13). This can be seen graphically in Fig. 5B, where under Nodal/Tgf-β inhibition the fraction of cells in state B show a linear dependence on the initial conditions, which is indicative of cell autonomous fate decisions. This is different from Wnt/Fgf inhibition, where the curves are still non-monotonous at 48 hpa (see Figs. S12 and S13). To further study the role of Nodal/Tgf-β signalling in cell-cell communication, we performed a mass spectrometry analysis of the molecular components of the extracellular space by collecting the supernatant of gastruloid media at 48 hpa (see Materials and Methods). Our analysis detected several proteins secreted during the first 48h by gastruloids including those involved in Nodal/Tgf-β pathway (Nodal and Lefty1) while proteins related to the Wnt or Fgf pathways were not detected (see Extended Data). Therefore, we propose that Nodal signalling is a key contributor to cell-cell communication during

gastruloid symmetry breaking.

Cell fate transitions and cellular rearrangements coordinate gastruloid symmetry breaking in silico

Previously we showed that the rates of cell differentiation and cell-cell rearrangements (given by the fusion rate, see Fig. 4B,C) are of the same order, suggesting that cell fate transitions and cell sorting occur at a similar timescale during symmetry breaking. In order to understand how those two processes coordinate to achieve symmetry breaking in gastruloids, we coupled our simplified three-state model with 3D agent-based computer simulations. In the simulations, cells mechanically interact with each other via effective pairwise radial forces. In addition, cell division and differentiation are incorporated as stochastic processes (see Materials and Methods and Appendix 2). Motivated by our experimental results showing differential mechanics between T+ and T- tissues, we included differential adhesion between T+ (B) and T- (A and C) tissues, which were assumed to share similar mechanical properties. Using experimentally inferred parameters from the cell-fate decision model, we successfully recapitulated the symmetry-breaking dynamics observed *in vitro* (Fig. 6A). The system was initialised with a pre-defined number of cells and a certain initial fraction of A and B cells. From 24 h to 36 h, cell sorting produced a transient core of mixed A and B cells surrounded by newly differentiated C-state cells (Fig. 6A). From 60 h to 72 h, the compact B-core moved to the periphery, driving clear polarisation of the aggregate (see Movie 1). The degree of polarisation was dependent on the initial ϕ fraction (Fig. 6B, left), consistent with our experimental results (Fig. S1). Moreover, the initial size of the aggregate had a clear effect on the polarisation dynamics, with larger aggregates exhibiting a delayed symmetry-breaking (Fig. 6B, right), as reported experimentally (*22, 23*) (Fig. 6C). We conclude that a combination of cell fate dynamics and cell sorting can account for gastruloid symmetry breaking.

Discussion

In this work, we provide a mechanochemical basis for symmetry breaking in gastruloids, taking into account cell fate transitions and collective cell rearrangements. By combining cell proportion experiments with mathematical modelling, we uncovered that cell fate decisions in gastruloids are not taken autonomously at the single-cell level, but instead emerge collectively at the population level. Notably, despite collective decision-making, we find that gastruloids are not robust to changes in the initial T+ population, in contrast to other developmental systems (*30*). This sensitivity to the initial conditions may explain the pronounced variability observed in gastruloids cultured under different medium conditions, leading to diverse cell type compositions (*26, 28, 32*). By screening a range of candidate models, we found that our experimental observations are best captured by a mechanism in which the pluripotent population slows down differentiation. Consistent with this picture, pathway perturbations and mass spectrometry analyses identify the Nodal/Tgf-β pathway as a likely mediator of cell-cell communication in the system. One possible hypothesis is that Lefty1 suppresses differentiation by modulating Nodal signalling in this system, analogous to its role in anteroposterior patterning in the mouse embryo (*6*). Further work will be required to directly test this hypothesis.

We further uncover spatial differences in T expression between the core and periphery of gastruloids prior to symmetry breaking. Specifically, at 48 hpa, T+ cells that subsequently lose T expression are predominantly located at the periphery of the aggregates. This transient radial organisation is reminiscent of recent work reporting early spatial heterogeneity in pluripotency in gastruloids before symmetry breaking (*29*), where primitive streak-like cells localised to the periphery while pluripotent-like cells occupied the core. One plausible mechanism underlying this radial patterning is cell sorting driven by differential adhesion (*39, 49–53*). Consistent with this interpretation, we observe mechanical differences between T+ and T- tissues, as well

as different cadherin levels, supporting the existence of adhesion-mediated sorting. Moreover, recent experiments tracking morphogen signalling dynamics have shown that, during gastruloid polarisation, single-cell Wnt activity predicts future cell position and that axis symmetry breaking likely emerges from sorting rearrangements driven by differential adhesion (*19*). Finally, by integrating cell fate dynamics with differential adhesion-based cell sorting *in silico*, we successfully recapitulate both the transient radial organisation observed at 48 hpa and the subsequent polarisation at 72 hpa (Fig. 6), as well as the size-dependent delay in symmetry breaking reported previously (*22, 23*).

Overall, our study suggests that not only cell-cell rearrangements, but also cellular feedback coordinates symmetry breaking in gastruloids. We propose a model where symmetry breaking occurs in two different stages: a sorting-dominated stage followed by a differentiation-dominated stage (see Fig. 6D). In the first stage (24-48 hpa), the pluripotent population slows down differentiation in the system via cellular feedback, thus allowing for T+ cells to preferentially sort and form a core before extensive differentiation. In a second stage (48-72 hpa), the pluripotent population is sufficiently low such that T+ cells can differentiate significantly, creating an outer crust of mesoderm-like cells which later helps the polarisation of the T+ core via differential tissue mechanics. Hence we argue that both cell fate transitions and mechanical forces orchestrate symmetry breaking following a common morphogenetic timescale. Indeed, recent work suggests that the coupling of cell signalling and differential adhesion is necessary for robust cell sorting (*54*). Understanding how multicellular systems integrate both biochemical and mechanical activities to ensure robust self-organisation will help us advance in the principles of biological self-organisation.

Materials and Methods

Transgenic mESC cell line maintanence

Bra/T::GFP mouse embryonic stem cells (*55*) were maintained in ESLIF medium, consisting of KnockOut Dulbecco's Modified Eagle Medium (DMEM) supplemented with 10% fetal bovine serum (FBS), 1x Non-essential aminoacids (NEEA), 50 U/mL Pen/Strep, 1x GlutaMax, 1x Sodium Pyruvate, 50 μM 2-Mercaptoethanol and leukemia inhibitory factor (LIF). Cells adhered to 0.1% gelatin-coated (Millipore, ES-006-B) tissue culture-treated 25 cm^2 or 75 cm^2 flasks (T25 Corning 353108; T75 Corning, 353136) in an incubator at 37 °C and 5% CO_2. Under these conditions, the percentage of T+ cells varied from 1 to 5% of the total population as determined by FACS.

Cell proportion experiments

Cells were cultured in two T75 culture flasks to a confluency of $\sim 50 - 80\%$. For the case of exogenous labelling, in the same day of FACS sorting, both flasks were washed with 15 mL $PBS^{+/+}$ and one of them was incubated with 12 mL NDiff227 media (N2B27) (Takara Bio, #Y40002) containing 1.6 μM SiR-DNA (Spirochrome, SC007) for 1h while the other was incubated with N2B27 only. Four different conditions were obtained: (1) T-, SiR-DNA+, (2) T-, (3) T+, SiR-DNA+ and (4), T+ in 2 mL Eppendorf tubes containing 1.2 mL N2B27. Subsequently, cells were mixed in different proportions and seeded in 96-well U-bottom plates (Greiner Cellstar, #650970) (375 cells per well). 96-well plates of mES cell aggregates were imaged using a PerkinElmer Opera Phenix® system using a x20 dry objective and N.A. 0.4 in confocal mode. A z-stack was acquired for every aggregate at 4 μm intervals.

In situ hybidization chain reaction

Gastruloids were harvested from round bottom 96-well plates and transferred to 1.5 mL Eppendorf tubes with wide-bore p200 RNAase free tips. N2B27 media was removed after 3 washes for 5 min each with 1ml DPBS$^{-/-}$ and then samples were fixed with cold 4% PFA in DPBS$^{-/-}$ and kept at 4°C overnight. The following day, PFA was removed from the samples by washing 3x 1mL DPBS$^{-/-}$. At this point the samples were kept at 4° up to a week. Next, the samples were dehydrdated and permeabilized with a series of 1 mL 100 % methanol (MeOH) washes (x4 10 min washes and x1 50 min wash at RT). The samples were rehydrated with a series of graded 1 mL MeOH/PBST (PBST: 1X PBS, 0.1% Tween 20) washes for 5 min each at RT (75/25, 50/50, 25/75, 5x 100/0). For the detection stage, a pre-hybridization step was done by adding 500 μL of probe hybridization buffer (PHB, Molecular Instruments) to the sample for 30 min at 37 °C. The probe solution was prepared by adding 0.4 pmol of each detection probe mixture to 500 μL of PHB. The pre-hybridization solution was removed and the probe solution was added and incubated overnight at 37°C. The next day the excess detection probes were removed by washing x4, 15 min with 500 μL probe was buffer (PWB, Molecular Instruments) which was pre-heated at 37°C. Next, the samples were washed twice for 5 min with 5 x SSCT (5x Sodium chloride sodium citrate, 0.1% Tween in water) at RT. For the amplification stage, a pre-amplification step was done by adding 500 μL of amplification buffer (Molecular Instruments) equilibrated at RT for 30 min. Next, 6 pmol of hairpins h1 and h2 1:1 were prepared by snap cooling 2 μL from a 3 μM stock (heated at 95°C for 90 s and cooled down to RT in the dark for 30 min). The hairpin mixture was prepared by diluting snap-cooled h1 and h2 hairpins to 1:250 in amplification buffer at RT. The amplification solution was removed from the sample and 250 μL of the hairpin mixture were added to each reaction to a final concentration of 12 nM for each hairpin. The samples were incubated at RT overnight. Finally, on the next day the excess hairpins were removed by washing with 500 μL 5x SSCT at RT (2 x 5 min, 2 x 30 min,

1 x 5 min). Samples were stored at 4°C protected from light before microscopy. Gastruloids were transferred to flat-bottom 96 well plates (PerkinElmer Cell Carrier - 96 Ultra) and were imaged using a PerkinElmer Opera Phenix® system using a x20 water and N.A. 1 in confocal mode. A z-stack was acquired for every aggregate at 4 μm intervals.

Cell lysis and Western blots

600-cell gastruloids were pulled together at 24 hpa from a 96-well plate ($\sim 6 \cdot 10^4$ cells). Gastruloids were treated with 0.05 % Trypsin-EDTA (Thermo Fisch der Scientific) for 3 min. The cell suspension was washed with 5 mL DPBS$^{+/+}$ and spun down for 3 min at 900 rpm twice to remove the excess Trypsin. Cells were washed twice with 5 mL ice-cold TBS-Ca^{++} buffer (5 mM $CaCl_2$, 50 mM TrisHCl pH 7.5, 150 mM NaCl) containing 1 mM PMSF in DMSO and spun down for 3 min at 900 rpm. Cells were subsequently washed with 5 mL ice-cold HBSS. Finally, 250 μL RIPA lysis buffer (500 mM TrisHCl pH 7.5, 10 mM EDTA, 1.5 M NaCl, 10 % v/v Np40 and 2.5 % m/v DOC) containing one tablet of protein inhibitor cocktail diluted 1:7 was added to the cell lysate and the cells were kept on ice for 15 min. The lysate was transferred into a micro-centrifuge tube and was shaken for 1h at 48°C. Finally, the lysate was passed through a Qia shredder and centrifuged at 15000 rpm) at 48°C for 15 min. At this point the lysate was flash frozen and stored at -20°C. To perform the Western blots, cell lysates were resolved on SDS-polyacrylamide gels (BIO-RAD Mini-Protean Precast Gels) and the proteins transferred onto nitrocellulose blotting membranes (Amersham). Membranes were blocked for 30 min at room temperature (RT) with 10 % (w/v) skimmed milk diluted in TBS (10 mM Tris-HCl [pH 7.4] and 100 mM NaCl)-0.1% Tween-20 (TBS-T), and then probed for overnight at 4°C with primary antibodies diluted in 5% skimmed milk in TBS-T. After several washes, the membranes were incubated at RT for 45 min with horseradish peroxidase-conjugated secondary antibodies (Invitrogen) diluted in 5% skimmed milk in TBS-T. Antibody

binding was detected by chemiluminiscence (ECL Prime Western Blotting Detection Reagent, Amersham) on a Fusion Fx Spectra Imager (Vilber). The antibodies used can be found in Table S2.

Image analysis

Image analysis was done using the software MOrgAna (*56*). In order to obtain the image masks, a custom-made Python scripts for downstream data processing were used. For the cell proportion experiments, average intensities were computed at the focal plane and the background signal was subtracted. For the radial analysis, we first pre-processed the sirDNA signal I_{sirDNA} for each aggregate by removing high intensity peaks corresponding to 0.3% of the total signal. Next, the relative intensity measure $\delta I = I_{\mathrm{sirDNA}}/\langle I_{\mathrm{sirDNA}}\rangle - I_{\mathrm{GFP}}/\langle I_{\mathrm{GFP}}\rangle$ was computed for each aggregate image, where the spatial average $\langle \ldots \rangle$ was performed in the masked region. The relative intensity radial profiles for each aggregate were obtained by counting the values δI in a set of pixels at a distance r from the center of mass of the aggregate and normalising by this value. Finally, in order to average the profiles over different aggregates, we first normalised the radial axis by interpolating the profiles. For the morphometric quantification of gastruloids, the software MOrgAna was used to straighten the gastruloids (see Ref. (*56*) for details) and the aspect ratio was defined as the ratio between the major axis L and minor axis d (see Fig. 1E and S1B). In order to quantify gastruloid polarisation, the averaged anteroposterior intensity profile $I(x)$ was obtained by analysing several gastruloids using the software, where x was the normalised anteroposterior axis such that $x \in [0, 1]$. Finally, the polarisation parameter P was defined as $P(x) = \int_0^1 I(x)(x - 1/2)dx / \int_0^1 I(x)$.

Nanoindentation and inference of mechanical parameters

The mechanical measurements were done using the Chiaro Nanoindenter (Optics11) adapted to a Leica DMi8 inverted microscope. The aggregates were transferred from the multiwell plates to μ-Slide 8 well coverslips (ibidi, #80826) coated with 0.1 % gelatin and containing warm N2B27. Indentations were done with a spherical cantilever probe of 27 ± 3 μm of radius and a stiffness of 0.025 ± 0.002 N m^{-1}. The approach speed was 5 μm s^{-1} and the indentation depth was $\simeq 6$ μm (~ 3 % of the typical size of an aggregate). The effective elastic modulus E_{eff} was calculated by fitting the Hertz's model to the indentation curves and the corresponding shear modulus was obtained as $\mu = (E_{\text{eff}}/2)(1-\nu^2)/(1+\nu)$, assuming a Poisson's ratio of $\nu = 1/2$. The average effective elastic modulus was obtained by averaging over the different aggregates. In order to obtain the effective surface tension γ and viscosity η of the cellular aggregates, the viscocapillary velocity γ/η and the elastocapillary length γ/μ were obtained by fitting a Kelvin-Voigt model to the fusion experiments in Fig. 4B,C as explained in Refs. (*36, 37*). Finally, by using the obtained value of the shear elastic modulus μ from the nanoindentation measurements, the parameters η and γ were inferred.

Cell fate model exploration and inference of cell fate transition rates

The experimental dataset (24, 48 and 72 hpa data) was fit to the model using 4 parameters, $\alpha = p/q$, K, τ_{24} and τ_{48}, where the last two parameters correspond to the dimensionless time-points at 24 hpa and 48 hpa. The reason why four parameters are needed instead of three (p, q, K) is because the seeding time ($\tau = 0$) does not correspond to the time when signalling starts. Hence, an additional time parameter is needed. The timescale of the process was then obtained as $24\,\text{h}/(\tau_{48} - \tau_{24})$. The dimensionless timepoint at 72 hpa was obtained as $\tau_{72} = 2\tau_{48} - \tau_{24}$. For the signalling perturbations, in some cases the model was simplified by considering no p-transitions or the absence of feedback ($K \to \infty$) (see Table S3). The 24,

48 and 72 hpa datasets were simultaneously fit to the analytical model using non-linear least squares fitting and leave-one-out cross-validation. Parameter sets yielding a z-score larger than 1 were discarded. The final fitted parameters (see Table S3) correspond to the mean values across fits, with errors given by the standard deviation. For the model exploration shown in Figs. S9 and S10, stochastic simulations were performed to find estimations of the mean values of $\phi_B(t)$ for all master equations, as closed-form solutions were not available for all 24 models. Each model was simulated with $N = 10^4$ independent realisations and five different proportions of A and B states to compute the mean values. Parameter fitting was performed using the NOMAD algorithm (*57*), with the loss defined as the absolute error between experimental means at each time point and simulation means. The parameter search space was $\alpha \in (0, 10), K \in (0, 10), \tau_{24} \in (0, 100), \tau_{48} \in (0, 100)$. The experimental data in Figs. 1 and S1A were fit to the analytical solution of the cell-cell communication model in which state A inhibits both AB and BC transitions (see Appendix Eqs. S15 and S16) using the `curve_fit` function from `scipy.optimize` in Python.

Single-cell RNA sequencing analysis

The 24 and 48 hpa scRNA sequencing data was used from previous work in Ref. (*32*). Next, we detail the different steps of the analysis:

Quality control, normalisation and scaling. We analysed each sample independently corresponding to a time point each. We calculated the standard quality control metrics of total counts per cell, number of expressed genes per cell, and mitochondrial fraction. We heuristically set quality control thresholds for each metric based on the observed bimodalities of the histogram plots. Cells outside the thresholds were removed from further analysis. In the following, we used scrublet algorithm (*58*) to impute candidate doublets. We estimated the scrublet

score threshold using the heuristic method described in the original paper, by observing the bimodality on the histogram of simulated doublets scrublet scores. Cells with scores above this threshold were imputed as doublets and removed from further analysis. The remaining cells in the count matrix were normalised to a total count sum of 10^5 counts. The analysis was insensitive to the specific choice of this parameter. In addition, the matrix was log-one-plus normalised before downstream analysis.

Feature selection, dimensionality reduction and visualisation. For dimensionality reduction genes were selected using the `scanpy.pp.highly_variable_genes` function with "seurat" flavor (*59*) and the top 2000 genes were used as input dimensions for a Principal Component Analysis (PCA). The results were insensitive to the specific number of top genes selected. With the PCA, we retained the 20 components with more explained variance. This choice was based on the selection of components by perfoming a randomisation test such that all datasets have the same number of components. The selection of components was also orientative and robust to the specific choice on the number of components. With the selected number of principal components, we generated a k-nearest neighbours (k-NN) graph representation of the data using the `scanpy.pp.neighbors` with correlation metric. UMAP plots were created for visualisation using the `scanpy.tl.umap` function with default parameters.

Annotation. For annotation, we used the marker genes appearing in Table S1. The custom annotation algorithm worked in two steps. First, cells that had at least one count of a marker gene were considered positive for the gene and negative only if there were no counts present. Each cell was assigned a fate if it expressed the combination of positive or negative markers for that specific fate. Cells that were annotated with more than one fate were treated as "Multi-assigned", and cells with no annotation as "Unassigned". In a second step, we trained a k-NN

classifier over the PCA space with the uniquely assigned cells as the training set and the ”Multi-assigned” and ”Unassigned” cell as prediction cells. These two sets of cells were annotated using the majority vote of the remaining k-NN 15 nearest neighbours.

Time sample integration. For integrating the time samples of each dataset we combined the samples after the quality control step. With this matrix, we normalised, scaled, selected features and performed the PCA analysis in the same procedure described above. With the retained PCA components, we used the `scanpy.external.pp.harmony` function to correct for the batch effect between samples. The corrected representation was then used for constructing the graphs, the UMAPs, clustering and annotation as described before.

Proteomics analysis

In the following section we detail the procedure used to perform the proteomic analysis of the secreted proteins in gastruloids:

Sample preparation. To identify proteins secreted by gastruloids, 600 cells/20 μL N2B27 media/well were seeded in a 96-well ULA plate (Greiner, 650970). For negative control the same amount of N2B27 (Takara, Y40002) media was kept. At 48 hpa, samples were collected as bulk and centrifuged at 900 rpm for 3 min. The supernatant and the control media were then filtered by Amicon Ultra-0.5 centrifugal filter unit (Merck, UFC500308) until volume was reduced to half. Three technical replicas (both for supernatant and the control media, 40 μL/well) were loaded onto separate SDS gels and stained with Coomassie blue. Gel pieces were excised (excluding BSA and proteins of similar size (55-75 kDa)) and proteins were subjected to in-gel digestion with trypsin. Next, gels band were destained with 100 mM NH_4HCO_3 in 40 % acetonitrile, reduced with dithiothreitol (2 μmol, 30 min, 56 °C), alkylated in the dark

with iodoacetamide (11 μmol, 30 min, 25 °C), dehydrated with acetonitrile for trypsin digestion (400 ng, 37 °C, 8h, Promega cat # V5113).After digestion, peptide mix was acidified with formic acid prior to LC-MS/MS analysis and desalted with a MicroSpin C18 column (The Nest Group, Inc) prior to LC-MS/MS analysis.

Chromatographic and mass spectrometric analysis. Samples were analysed using a Orbitrap Fusion Lumos mass spectrometer (Thermo Fisher Scientific, San Jose, CA, USA) coupled to an EASY-nLC 1200 (Thermo Fisher Scientific (Proxeon), Odense, Denmark). Peptides were loaded directly onto the analytical column and were separated by reversed-phase chromatography using a 50-cm column with an inner diameter of 75 μm, packed with 2 μm C18 particles (Thermo Fisher Scientific, cat # ES903). Chromatographic gradients started at 95% buffer A and 5% buffer B with a flow rate of 300 nl/min and gradually increased to 25% buffer B and 75% A in 79 min and then to 40% buffer B and 60% A in 11 min. After each analysis, the column was washed for 10 min with 100% buffer B. Buffer A: 0.1% formic acid in water. Buffer B: 0.1% formic acid in 80% acetonitrile. The mass spectrometer was operated in positive ionisation mode with nanospray voltage set at 2.4 kV and source temperature at 305°C. The acquisition was performed in data-dependent acquisition (DDA) mode and full MS scans with 1 micro scans at resolution of 120,000 were used over a mass range of m/z 350-1400 with detection in the Orbitrap mass analyser. Auto gain control (AGC) was set to 'standard' and injection time to 'auto'. In each cycle of data-dependent acquisition analysis, following each survey scan, the most intense ions above a threshold ion count of 10000 were selected for fragmentation. The number of selected precursor ions for fragmentation was determined by the "Top Speed" acquisition algorithm and a dynamic exclusion of 60 seconds. Fragment ion spectra were produced via high-energy collision dissociation (HCD) at normalised collision energy of 28 % and they were acquired in the ion trap mass analyser. AGC and injection time were set

to 'Standard' and 'Dynamic', respectively and isolation window of 1.4 m/z was used. Digested bovine serum albumin (New England biolabs cat # P8108S) was analysed between each sample to avoid sample carryover and to assure stability of the instrument and QCloud has been used to control instrument longitudinal performance during the project.

Data analysis. Acquired spectra were analysed using the Proteome Discoverer software suite (v2.5, Thermo Fisher Scientific) and the Mascot search engine (v2.6, Matrix Science). The data were searches against a Swiss-Prot mouse database (as in March 2021, 17238 entries) plus a list of common contaminants and all the corresponding decoy entries. For peptide identification a precursor ion mass tolerance of 7 ppm was used for MS1 level, trypsin was chosen as enzyme and up to three missed cleavages were allowed. The fragment ion mass tolerance was set to 0.5 Da for MS2 spectra. Oxidation of methionine and N-terminal protein acetylation were used as variable modifications whereas carbamidomethylation on cysteines was set as a fixed modification. False discovery rate (FDR) in peptide identification was set to a maximum of 1%.

Agent-based simulations

Simulations were performed using the Julia package `CellBasedModels.jl` (https://github.com/dsb-lab/CellBasedModels.jl). A center-based model was used to describe the dynamics of each cell in the aggregate taking into account repulsion and adhesion forces, as well as friction forces between cells (*60*) (Appendix S2). In addition, cells proliferated and differentiated according to the three-state differentiation model described in the Main Text (see Appendix S1). Polarisation was quantified as the normalised distance between the center of mass of the largest T+ (B-type) cluster and that of the entire aggregate. Simulations were run for times up to 96 h signalling time (the time elapsed since the onset of cell differentiation) covering the time window of the *in vitro* experiments. Starting from an initial aggregate size

of 300 cells we simulated cases with initial fractions of T+ cells of 0%, 20%, 50%, and 80%. To examine the effect of the initial aggregate size, additional simulations were performed with initial aggregate sizes of 300, 600, and 900 cells and $\phi = 0\%$. For each case, 10 independent simulations were run to ensure statistical robustness.

Code availability

All scRNA-seq analysis was performed in Python. The scripts can be found in github (https://github.com/dsb-lab/gastruloids_positive_feedback_scRNAseq_analysis). To mantain reproducibility, we performed the analysis using a docker image containing all the required software to reproduce the analysis, provided in Dockerhub (https://hub.docker.com/r/dsblab/single_cell_analysis), and using the v0.6 image. Fitting of the mean field model was performed using Julia. The scripts can be found in github (https://github.com/dsb-lab/gastruloids_positive_feedback_mean_field_fitting).

Acknowledgments

We thank S. Gsell, P.-F. Lenne, A. Martinez Arias, V. Ruprecht, J. Sharpe, K. Stapornwongkul and V. Weichselberger for critical reading of the manuscript. We thank the Mesoscopic Imaging Facility (EMBL Barcelona) for assistance with imaging and the Tissue Engineering Unit (CRG) for culture media preparation. The proteomics analyses were performed in the CRG/UPF Proteomics Unit which is part of the Spanish National Research Infrastructure ICTS OmicsTech. D.O. acknowledges funding from Juan de la Cierva Incorporación with Project no. IJC2018-035298-I from the Spanish Ministry of Science, Innovation and Universities (MCIU/AEI). D.O, S.S., J.G.-O., and V.T acknowledge funding by the Spanish Ministry of Science and Innovation and FEDER, under projects FIS2017-92551-EXP, PID2021-128269NA-I00, PID2024-160263NB-I00, by the “Maria de Maeztu” Program for Units of Excellence in R&D (grant

CEX2024-001431-M), and by the Generalitat de Catalunya (ICREA Academia program). G.T-C. was supported by an FPU doctoral fellowship from the Spanish Ministry of Education and Universities (reference FPU18/05091) and an EIPOD4 fellowship under the Marie Skłodowska-Curie Actions COFUND 4 (847543). S.S. acknowledges funding from the ARISE2 program funded by the European Union's Horizon Europe research and innovation programme under the Marie Skłodowska-Curie grant agreement with No 101178241. This work was supported by funds from EMBL and ERC-2022-SYG (101072123) to V.T, and ERC-2024-SYG (101167121) to J.G.O. We thank all the members of the Trivedi group for feedback on the project.

Author contributions

Conceived and designed the experiments: D.O., V.T. Performed the experiments: D.O., Kr.A., D.F.-M., E.H., Ke.A. Analyzed the data: D.O., G.T.-C., S.S, J.G.-O. Contributed materials/analysis tools: D.O., G.T.-C., S.S, J.G.-O., V.T. Wrote the paper: D.O., G.T.-C., S.S., J.G.-O., V.T.

Main Figures

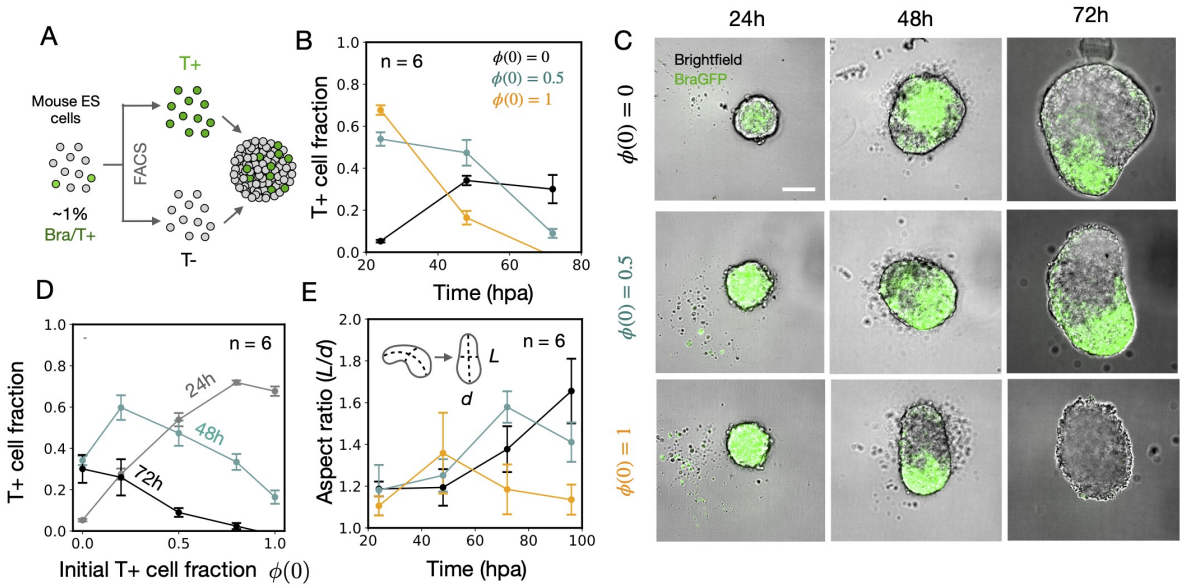

Figure 1: **T dynamics under controlled cell proportions.** A) Schematics of the cell proportion experiments. mESCs were cultured in 2D under ESLIF conditions, and were subsequently FACS sorted into T+ and T- populations. The different cell populations were mixed in different proportions to form 3D aggregates in multi-well 96 plates in N2B27 medium. B) Time evolution of the T+ fraction for different starting T+ populations $\phi(0) = 0, 0.5, 1$. C) Representative brightfield images of the aggregates at 24, 48 and 72 hpa for initial T+ fractions $\phi(0) = 0, 0.5, 1$. The images are composed with the signal from a GFP reporter of T expression. Scale bar: 200 μm. D) T+ cell fraction as a function of the initial fraction of T+ cells ϕ for 24, 48 and 72 hpa. In each experiment approximately 50 cell aggregates were analysed. The fraction of T+ cells was obtained by normalising by the extrapolated GFP intensity at $\phi = 1$ at 24 hpa. E) Time evolution of the aspect ratio of gastruloids for initial T+ fractions $\phi(0) = 0, 0.5, 1$. Error bars in panels B and D correspond to $2 \times$ SEM over $n = 6$ replicates. In each replicate ~ 10 aggregates were averaged for each condition. Error bars in E indicate SD.

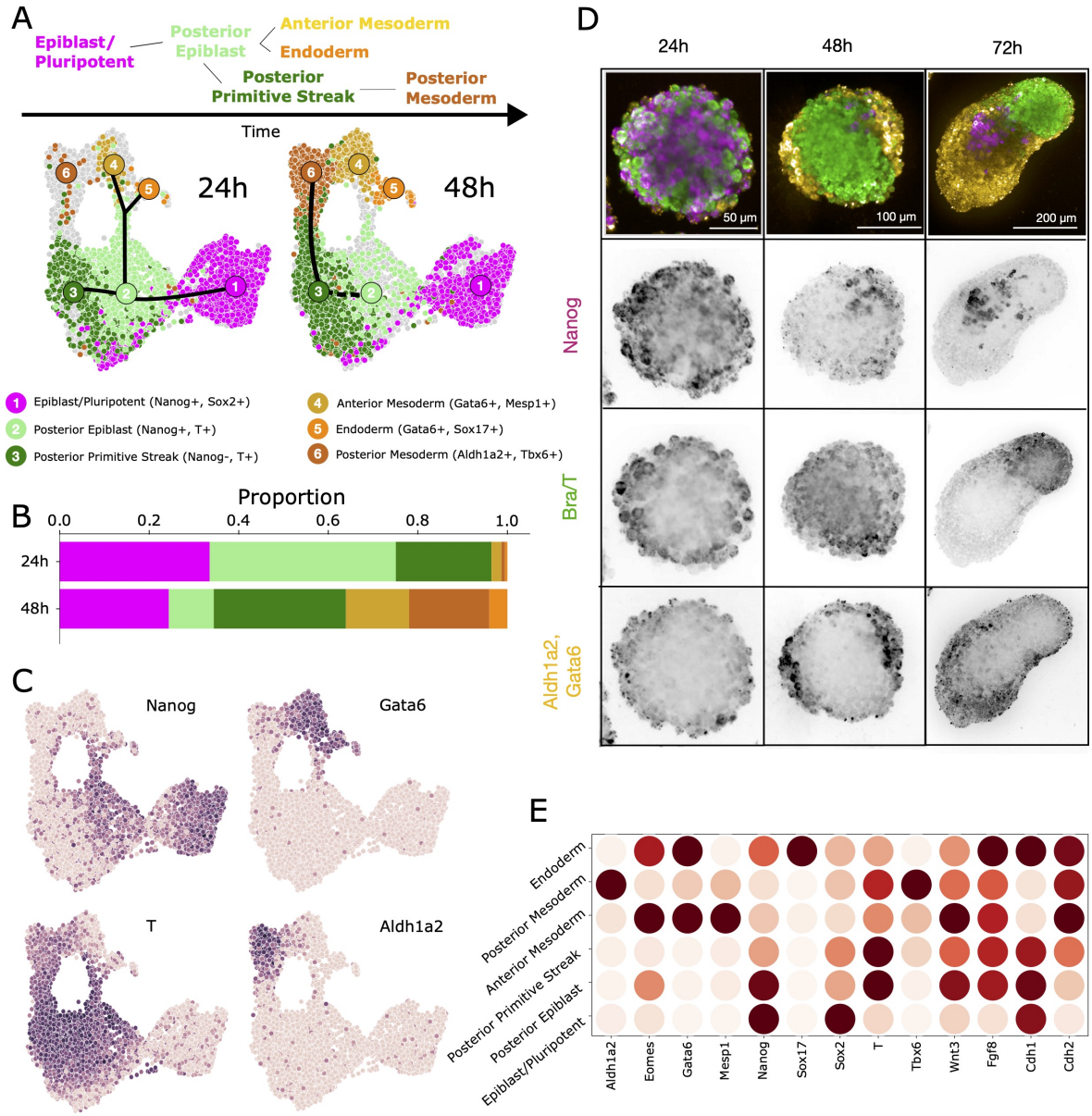

Figure 2: **Cell fate dynamics during early gastruloid differentiation**. A) Integrated UMAP of 24 hpa and 48 hpa: light gray indicates combined data and colored points correspond to individual timepoints showing how the different states are populated over time. B) The corresponding proportions by annotation are shown. C) UMAPs showing expression of selected genes. D) HCR stainings for the 3 main cellular states at 24, 48 and 72 hpa: Nanog+ pluripotent state, a T+ primitive streak-like state and further differentiated states being Aldh1a2+ and Gata6+. E) Mean normalised and log-normalised gene expression per cluster of relevant genes per annotation cluster at 48 hpa.

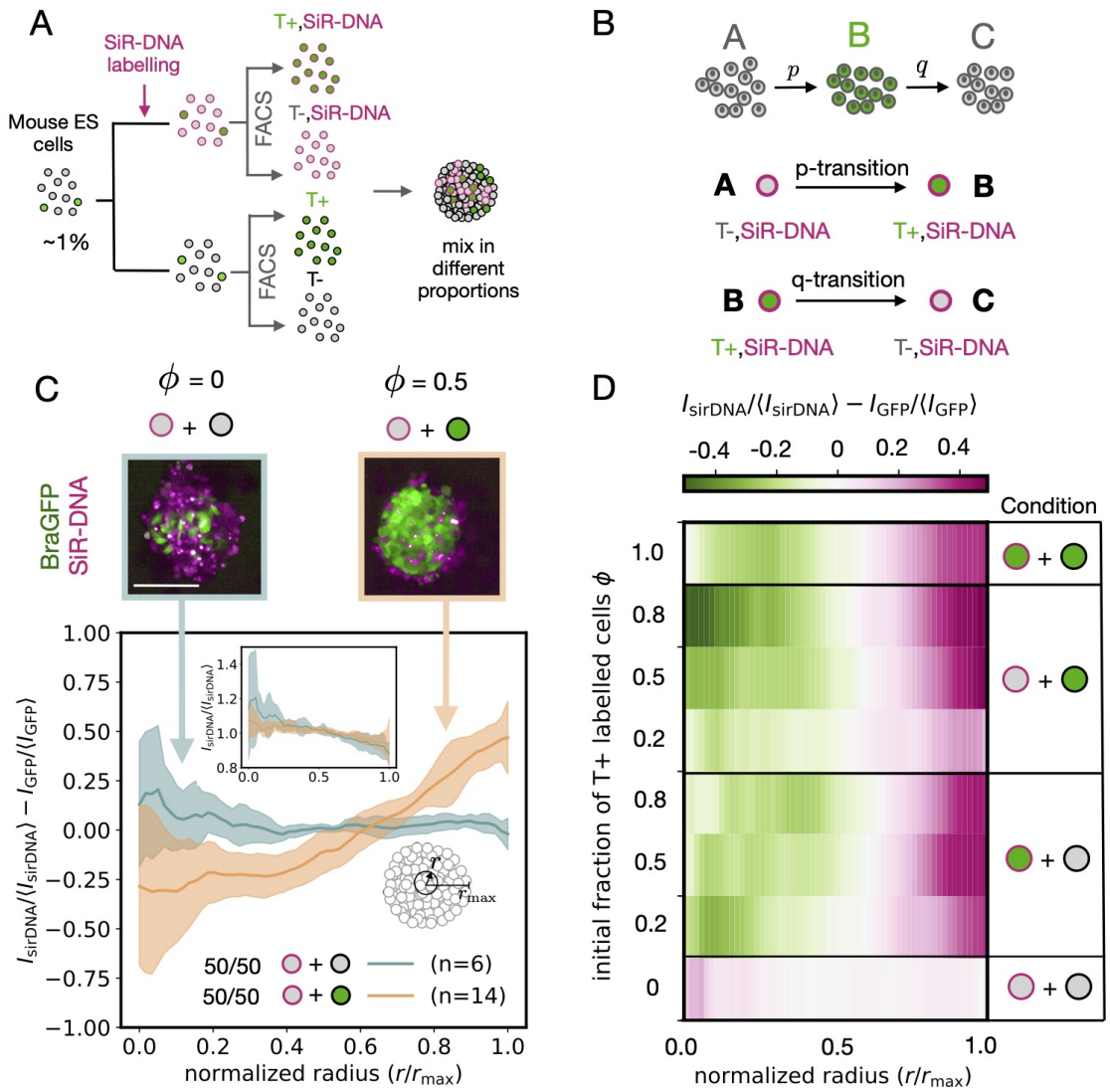

Figure 3: **Spatial organisation of T in cell proportion experiments** A) Schematics of the cell proportions experiment with exogenous labelling. mESCs were cultured in 2D under ESLIF conditions and a certain fraction was labelled with SiR-DNA for 1h. Cells were subsequently FACS sorted into four different populations: (1) T+, SiR-DNA+; (2) T-, SiR-DNA+; (3) T+, SiR-DNA- and (4) T-, SiR-DNA-. Finally, the different cell populations were mixed in different proportions to form 3D aggregates in multi-well 96 plates in N2B27 medium and studied at 24 hpa. B) SiR-DNA labelling of the T- cells allowed us to detect p-transitions while labelling of T+ cells allowed us to detect q-transitions. C) Cell proportion experiments mixing 50/50 populations of labelled and unlabelled cells. When the cell populations are different, T- cells are enriched on the surface of the aggregate. Radial intensity profile showing GFP enrichment in the inner part of the aggregate relative to SiR-DNA signal. Inset: Radial SiR-DNA signal profile showing no significant spatial organisation. Images correspond to confocal maximum intensity projections at 24 hpa. Shaded error bars correspond to SD. D) Colormaps of the radial profile for different starting fractions of T+ cells ϕ as well as different populations labelled with SiR-DNA. In the inner part of the aggregate the majority of cells are in state B, while in the periphery the majority of cells are in either A or C states.

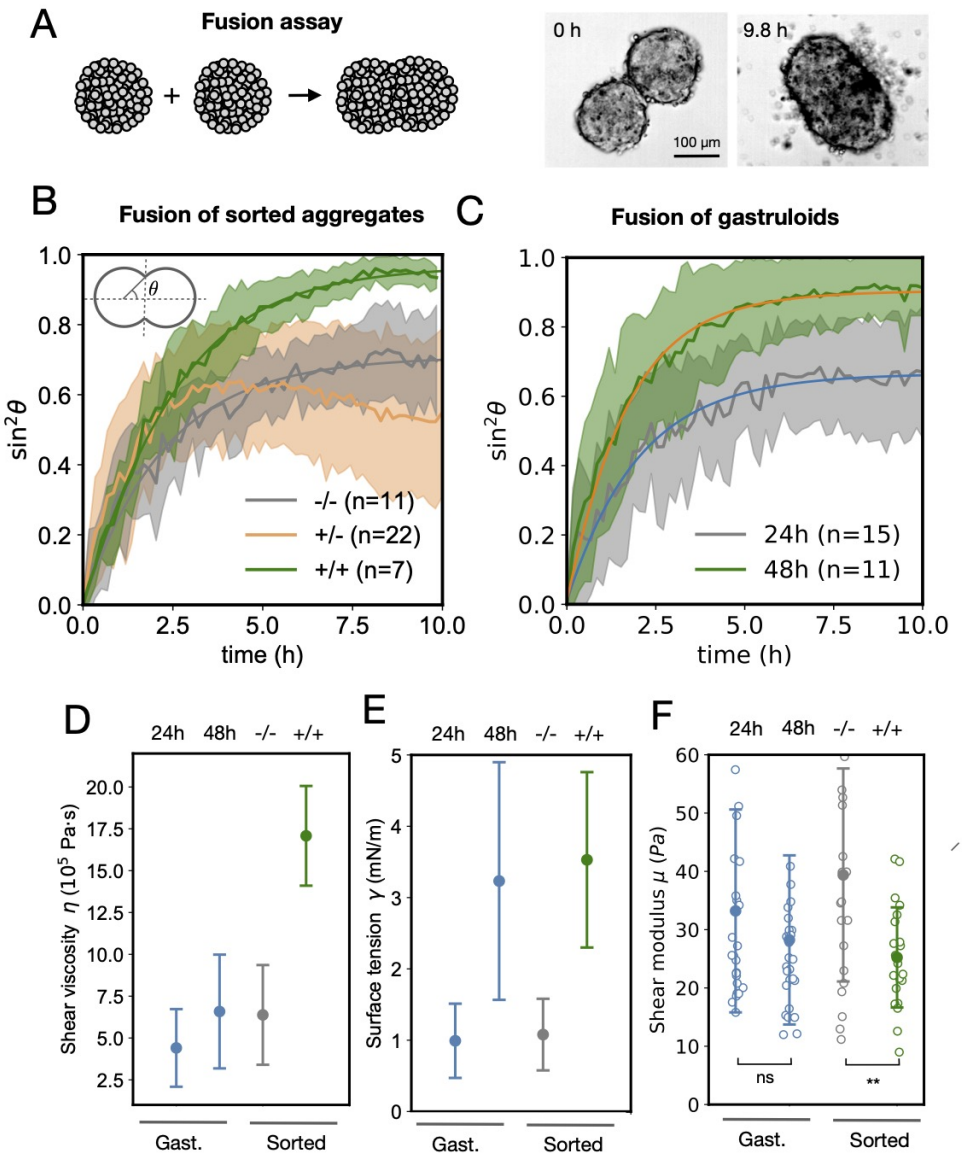

Figure 4: **T expression impacts the mechanics of cellular aggregates** A) Fusion assay. Brightfield images of two fusing T- sorted aggregates before and after fusion. B) Time evolution of $\sin^2\theta$, where θ corresponds to the contact angle between the two aggregates (see inset). The average curves correspond to homotypic (T+/T+, T-/T-) and heterotypic (T+/T-) fusions of T+ and T- sorted aggregates.The average radius of T- and T+ aggregates was 80 $\pm$ 6 μm and 88 $\pm$ 6 μm, respectively (mean $\pm$ SD). n corresponds the number of analysed aggregates per condition. C) Time evolution of $\sin^2\theta$ for the fusion of 24 hpa and 48 hpa gastruloids. The average radius of 24 hpa and 48 hpa gastruloids was $R = 100 \pm 7$ μm and $R = 145 \pm 11$ μm, respectively (mean $\pm$ SD). Solid lines correspond to fits to a mathematical model considering the aggregates behave as Kelvin-Voigt materials. D, E) Inferred effective tissue shear viscosity η and surface tension γ for gastruloids, T+ and T- aggregates. F) Nanoindentation measurements of the shear elastic modulus μ for gastruloids, T+ and T- aggregates. ** $P < 0.01$, both t-test and Mann-Whitney U test. ns: both t-test and Mann-Whitney U test. The number n corresponds to number of fusion events. Shaded error bars correspond to SD.

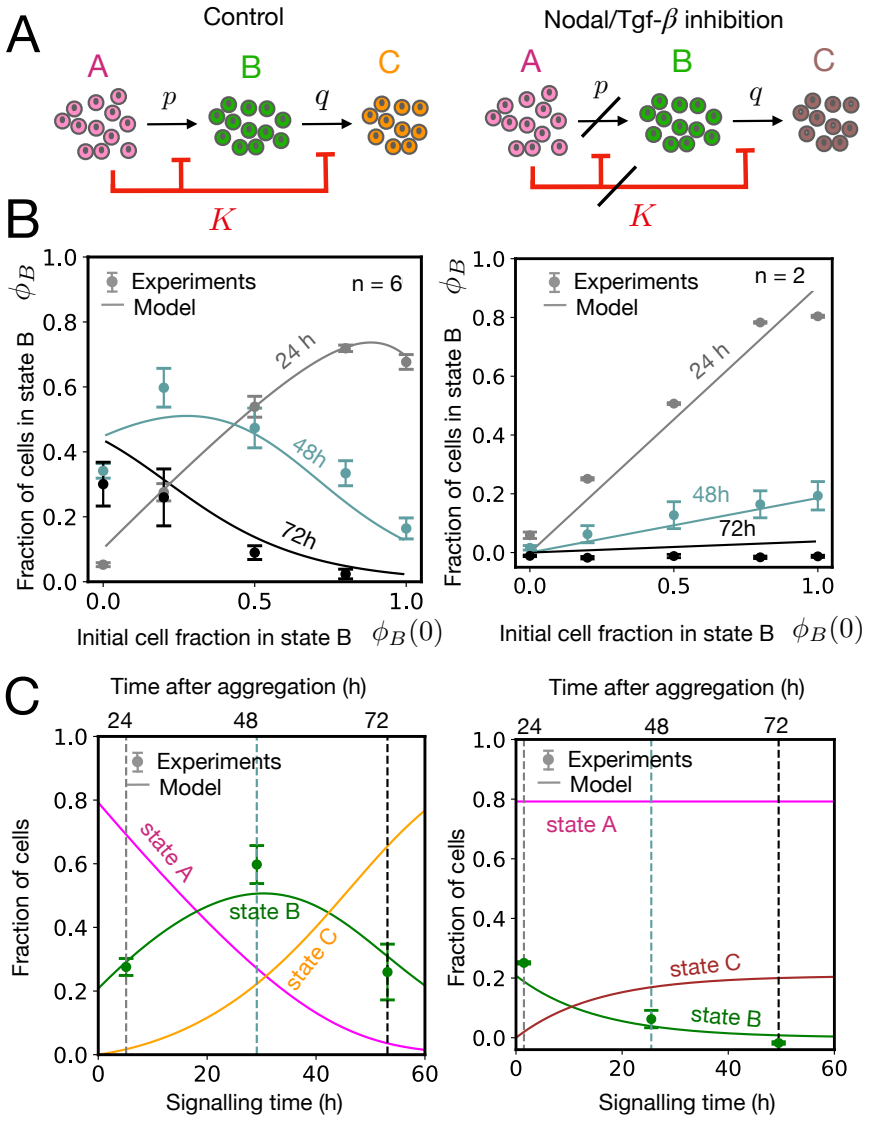

Figure 5: **Cell-cell communication explains cell fate dynamics in gastruloids**. A) Minimal cell-cell signalling model considering cells transition through 3 main cellular states (A, B and C). State A is assumed to prevent cell differentiation from A to B and from B to C with feedback strength K. In principle, given that the inhibitory signals might affect cell differentiation, we denote state C with a different color (brown). B) Evolution of the fraction of cells in state B as a function of the initial fraction of cells in state B for 24, 48 and 72 hpa. The fraction of cells in state B was obtained by normalising the GFP intensity by the extrapolated intensity at $\phi_B = 1$ at 24 hpa. Solid lines correspond to the fits using the models in panel A (see Appendix). The fitted parameters for the control case (left) are $p = 0.14 \pm 0.01$ h^{-1}, $q = 0.071 \pm 0.003$ h^{-1} and $K = 0.17 \pm 0.02$ (mean $\pm$ SD). For the Nodal/Tgf-β-inhibited case, the fit was obtained assuming $p = 0$ and $K \to \infty$ (no feedback) leading to $q = 0.0660 \pm 0.0004$ h^{-1}. Error bars correspond to $2 \times$ SEM over different replicates without the addition of SiR-DNA. In each replicate ~ 10 aggregates were averaged for each condition. C) Time evolution of the three states considering $\phi_A(0) = 0.8$, $\phi_B(0) = 0.2$, $\phi_C(0) = 0$ and using the fitted parameters from the experiments (see Materials and Methods). Vertical dashed lines indicate 24, 48 and 72 hpa while the x-axis corresponds to the signalling time. The initial timepoint $t = 0$ is inferred from the fit (see Materialss and Methods).

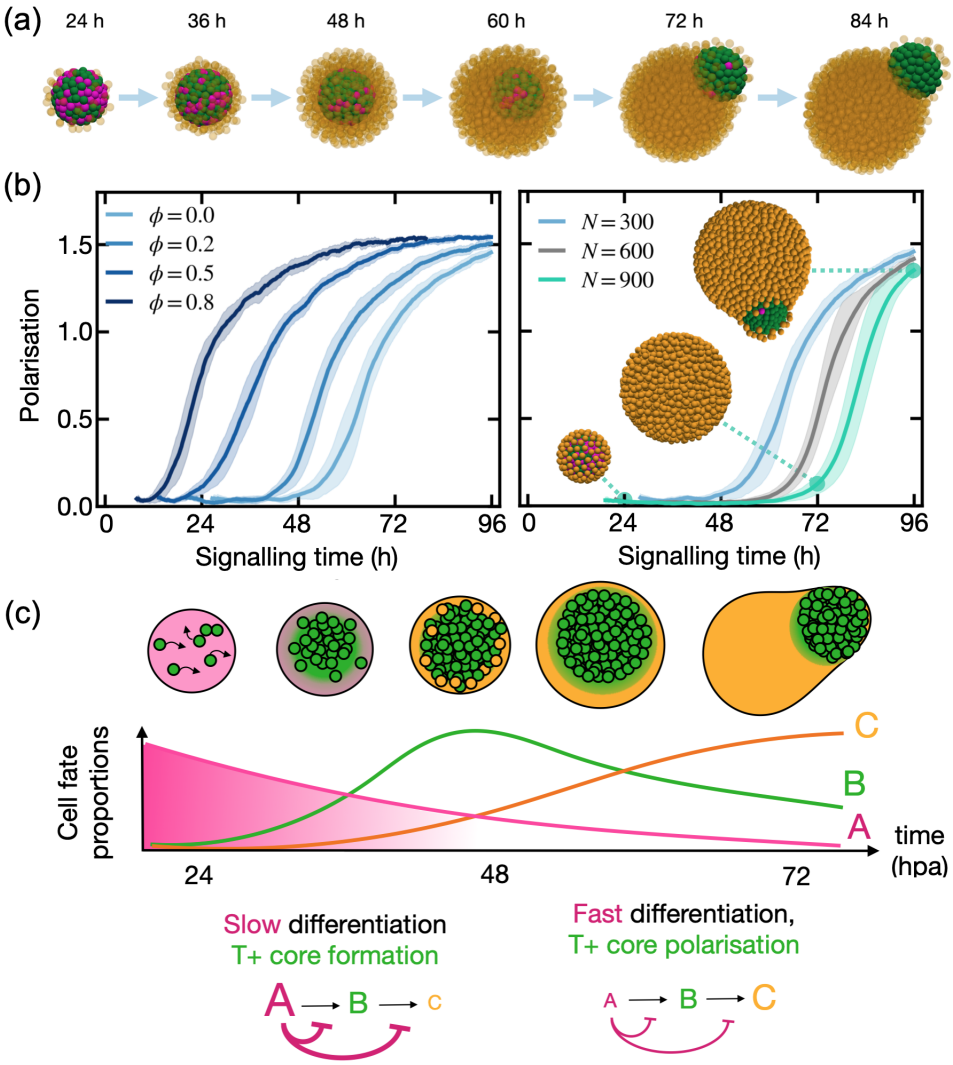

Figure 6: **The interplay of cell fate dynamics and cell sorting explains gastruloid symmetry breaking** (A) Representative snapshots of a 3D agent-based simulation of gastruloid symmetry-breaking considering cell-cell mechanical interactions, cell proliferation and cell differentiation. Cells interact with each other depending on their cellular fate (A, B or C) adhering to one another and driving cell-cell rearrangements. (B) Polarisation vs time. Left: Initial aggregate size $N = 300$ and different initial T+ starting fractions ϕ. Right: Polarisation vs time for different initial number of cells at 0 h and initial T+ starting fraction $\phi = 0$. Larger aggregates polarise slower than smaller ones. Polarisation is measured as the normalised center-of-mass distance between the B-cluster and the entire aggregate. The normalisation is done with respect to the size of the largest C-cluster (see Appendix S2). For each condition, mean $\pm$ SD is shown for 10 different simulations. (C) We propose that symmetry breaking is achieved in two stages: a first stage, where the pluripotent population slows down differentiation through cellular feedback and allows for T+ core formation through cell sorting, and a second stage where differentiation of T+ cells to the C state is sped up, leading to the polarisation process.

References

1. Christian P Petersen and Peter W Reddien. Wnt signaling and the polarity of the primary body axis. *Cell*, 139(6):1056–1068, 2009.

2. Kyle M Loh, Renée van Amerongen, and Roel Nusse. Generating cellular diversity and spatial form: Wnt signaling and the evolution of multicellular animals. *Developmental cell*, 38(6):643–655, 2016.

3. Christiane Nüsslein-Volhard and Eric Wieschaus. Mutations affecting segment number and polarity in drosophila. *Nature*, 287(5785):795–801, 1980.

4. Toshiro Mizuno, Etsuro Yamaha, Atsushi Kuroiwa, and Hiroyuki Takeda. Removal of vegetal yolk causes dorsal deficencies and impairs dorsal-inducing ability of the yolk cell in zebrafish. *Mechanisms of development*, 81(1-2):51–63, 1999.

5. S-R Chen and David Kimelman. The role of the yolk syncytial layer in germ layer patterning in zebrafish. *Development*, 127(21):4681–4689, 2000.

6. W Ross Waldrip, Elizabeth K Bikoff, Pamela A Hoodless, Jeffrey L Wrana, and Elizabeth J Robertson. Smad2 signaling in extraembryonic tissues determines anterior-posterior polarity of the early mouse embryo. *Cell*, 92(6):797–808, 1998.

7. Nikolas Uez, Heiko Lickert, Jürgen Kohlhase, Martin Hrabe de Angelis, Ralf Kühn, Wolfgang Wurst, and Thomas Floss. Sall4 isoforms act during proximal–distal and anterior–posterior axis formation in the mouse embryo. *Genesis*, 46(9):463–477, 2008.

8. Keisuke Ishihara and Elly M Tanaka. Spontaneous symmetry breaking and pattern formation of organoids. *Current Opinion in Systems Biology*, 11:123–128, 2018.

9. Derk ten Berge, Wouter Koole, Christophe Fuerer, Matt Fish, Elif Eroglu, and Roel Nusse. Wnt signaling mediates self-organization and axis formation in embryoid bodies. *Cell stem cell*, 3(5):508–518, 2008.

10. Susanne C Van den Brink, Peter Baillie-Johnson, Tina Balayo, Anna-Katerina Hadjantonakis, Sonja Nowotschin, David A Turner, and Alfonso Martinez Arias. Symmetry breaking, germ layer specification and axial organisation in aggregates of mouse embryonic stem cells. *Development*, 141(22):4231–4242, 2014.

11. Nozomu Takata, Eriko Sakakura, Mototsugu Eiraku, Takeya Kasukawa, and Yoshiki Sasai. Self-patterning of rostral-caudal neuroectoderm requires dual role of fgf signaling for localized wnt antagonism. *Nature communications*, 8(1):1–16, 2017.

12. Andrea Meinhardt, Dominic Eberle, Akira Tazaki, Adrian Ranga, Marco Niesche, Michaela Wilsch-Bräuninger, Agnieszka Stec, Gabriele Schackert, Matthias Lutolf, and Elly M Tanaka. 3d reconstitution of the patterned neural tube from embryonic stem cells. *Stem cell reports*, 3(6):987–999, 2014.

13. David A Turner, Mehmet Girgin, Luz Alonso-Crisostomo, Vikas Trivedi, Peter Baillie-Johnson, Cherise R Glodowski, Penelope C Hayward, Jérôme Collignon, Carsten Gustavsen, Palle Serup, et al. Anteroposterior polarity and elongation in the absence of extra-embryonic tissues and of spatially localised signalling in gastruloids: mammalian embryonic organoids. *Development*, 144(21):3894–3906, 2017.

14. Leonardo Beccari, Naomi Moris, Mehmet Girgin, David A Turner, Peter Baillie-Johnson, Anne-Catherine Cossy, Matthias P Lutolf, Denis Duboule, and Alfonso Martinez Arias. Multi-axial self-organization properties of mouse embryonic stem cells into gastruloids. *Nature*, 562(7726):272, 2018.

15. Naomi Moris, Kerim Anlas, Susanne C van den Brink, Anna Alemany, Julia Schröder, Sabitri Ghimire, Tina Balayo, Alexander van Oudenaarden, and Alfonso Martinez Arias. An in vitro model of early anteroposterior organization during human development. *Nature*, 582(7812):410–415, 2020.

16. JD Frenster, S Babin, JB Josende Garcia, P Casani Galdon, P Pascual-Mas, G Robertson, J Garcia Ojalvo, and A Martinez Arias. A mosaic gastruloid model highlights the developmental stage-specific restriction of cell competition in mammalian pre-gastrulation. *bioRxiv*, pages 2025–01, 2025.

17. David G Wilkinson, Sangita Bhatt, and Bernhard G Herrmann. Expression pattern of the mouse t gene and its role in mesoderm formation. *Nature*, 343(6259):657–659, 1990.

18. Ali Hashmi, Sham Tlili, Pierre Perrin, Molly Lowndes, Hanna Peradziryi, Joshua M Brickman, Alfonso Martínez Arias, and Pierre-François Lenne. Cell-state transitions and collective cell movement generate an endoderm-like region in gastruloids. *Elife*, 11:e59371, 2022.

19. Harold M McNamara, Sabrina C Solley, Britt Adamson, Michelle M Chan, and Jared E Toettcher. Recording morphogen signals reveals mechanisms underlying gastruloid symmetry breaking. *Nature Cell Biology*, pages 1–13, 2024.

20. Simon Gsell, Sham Tlili, Matthias Merkel, and Pierre-François Lenne. Marangoni-like tissue flows enhance symmetry breaking of embryonic organoids. *Nature Physics*, pages 1–10, 2025.

21. Melody Merle, Leah Friedman, Corinne Chureau, Armin Shoushtarizadeh, and Thomas Gregor. Precise and scalable self-organization in mammalian pseudo-embryos. *Nature Structural & Molecular Biology*, pages 1–7, 2024.

22. Isma Bennabi, Pauline Hansen, Melody Merle, Judith Pineau, Lucille Lopez-Delisle, Dominique Kolly, Denis Duboule, Alexandre Mayran, and Thomas Gregor. Size-dependent temporal decoupling of morphogenesis and transcriptional programs in gastruloids. *bioRxiv*, pages 2024–12, 2024.

23. Ulla-Maj Fiuza, Sara Bonavia, Pau Pascual-Mas, Gabriel Torregrosa-Cortes, Pablo Casani-Galdon, Gaelle Robertson, Andre Dias, and Alfonso Martinez Arias. Morphogenetic constrains in the development of gastruloids: implications for mouse gastrulation. *bioRxiv*, pages 2024–12, 2024.

24. Jesse V Veenvliet, Pierre-François Lenne, David A Turner, Iftach Nachman, and Vikas Trivedi. Sculpting with stem cells: how models of embryo development take shape. *Development*, 148(24):dev192914, 2021.

25. Lara Avni, Naama Farag, Binita Ghosh, and Iftach Nachman. Gastruloid optimization. *Emerging Topics in Life Sciences*, 7(4):409–415, 2023.

26. Kerim Anlas, Fumio Nakaki, Nicola Gritti, Jordi Font-Reverter, Krisztina Arató, Martí Planasdemunt-Hospital, David Oriola, James Sharpe, and Vikas Trivedi. Axial patterning of gastruloids via diverse cell type compositions. *bioRxiv*, pages 2025–03, 2025.

27. Marloes Blotenburg, Lianne Suurenbroek, Danique Bax, Joëlle de Visser, Vivek Bhardwaj, Luca Braccioli, Elzo de Wit, Antonius van Boxtel, Hendrik Marks, and Peter Zeller. Stem cell culture conditions affect in vitro differentiation potential and mouse gastruloid formation. *PloS one*, 20(3):e0317309, 2025.

28. Leah U Rosen, L Carine Stapel, Ricard Argelaguet, Charlie George Barker, Andrian Yang, Wolf Reik, and John C Marioni. Inter-gastruloid heterogeneity revealed by single cell

transcriptomics time course: implications for organoid based perturbation studies. *bioRxiv*, pages 2022–09, 2022.

29. Simon Suppinger, Marietta Zinner, Nadim Aizarani, Ilya Lukonin, Raphael Ortiz, Chiara Azzi, Michael B Stadler, Stefano Vianello, Giovanni Palla, Hubertus Kohler, et al. Multimodal characterization of murine gastruloid development. *Cell Stem Cell*, 30(6):867–884, 2023.

30. Néstor Saiz, Laura Mora-Bitria, Shahadat Rahman, Hannah George, Jeremy P Herder, Jordi García-Ojalvo, and Anna-Katerina Hadjantonakis. Growth-factor-mediated coupling between lineage size and cell fate choice underlies robustness of mammalian development. *Elife*, 9:e56079, 2020.

31. Kerim Anlas, Peter Baillie-Benson, Krisztina Arató, David A Turner, and Vikas Trivedi. Gastruloids: embryonic organoids from mouse embryonic stem cells to study patterning and development in early mammalian embryos. *Programmed Morphogenesis: Methods and Protocols*, pages 131–147, 2021.

32. Kerim Anlaş, Nicola Gritti, Fumio Nakaki, Laura Salamó Palau, Sham Leilah Tlili, David Oriola, Krisztina Arató, Jia Le Lim, James Sharpe, and Vikas Trivedi. Early autonomous patterning of the anteroposterior axis in gastruloids. *Development*, 151(22), 2024.

33. Kristina S Stapornwongkul, Elisa Maria Hahn, Laura Salamo Palau, Krisztina Arato, Nicola Gritti, Kerim Anlas, Patryk Polinski, Mireia Lopez, Miki Ebisuya, and Vikas Trivedi. Metabolic control of germ layer proportions through regulation of nodal and wnt signalling. *bioRxiv*, pages 2023–12, 2023.

34. Jimmy Tsz Hang Lee and Martin Hemberg. Supervised clustering for single-cell analysis. *Nature methods*, 16(10):965–966, 2019.

35. Sebastian J Arnold and Elizabeth J Robertson. Making a commitment: cell lineage allocation and axis patterning in the early mouse embryo. *Nature reviews Molecular cell biology*, 10(2):91–103, 2009.

36. David Oriola, Miquel Marin-Riera, Kerim Anlaş, Nicola Gritti, Marina Sanaki-Matsumiya, Germaine Aalderink, Miki Ebisuya, James Sharpe, and Vikas Trivedi. Arrested coalescence of multicellular aggregates. *Soft Matter*, 18:3771–3780, 2022.

37. Sotiris Samatas, Martí Planasdemunt-Hospital, and David Oriola. Arrested coalescence: A tool to explore tissue rheology. *Biophysica*, 4(4):604–618, 2024.

38. Malcolm S Steinberg. Adhesion-guided multicellular assembly: a commentary upon the postulates, real and imagined, of the differential adhesion hypothesis, with special attention to computer simulations of cell sorting. *Journal of theoretical biology*, 55(2):431–443, 1975.

39. Ramsey A Foty and Malcolm S Steinberg. The differential adhesion hypothesis: a direct evaluation. *Developmental biology*, 278(1):255–263, 2005.

40. Jennifer M Halbleib and W James Nelson. Cadherins in development: cell adhesion, sorting, and tissue morphogenesis. *Genes & development*, 20(23):3199–3214, 2006.

41. Akinao Nose, Akira Nagafuchi, and Masatoshi Takeichi. Expressed recombinant cadherins mediate cell sorting in model systems. *Cell*, 54(7):993–1001, 1988.

42. Nicolaas Godfried Van Kampen. *Stochastic processes in physics and chemistry*, volume 1. Elsevier, 1992.

43. Patrick S Stumpf, Rosanna CG Smith, Michael Lenz, Andreas Schuppert, Franz-Josef Müller, Ann Babtie, Thalia E Chan, Michael PH Stumpf, Colin P Please, Sam D How-

ison, et al. Stem cell differentiation as a non-markov stochastic process. *Cell Systems*, 5(3):268–282, 2017.

44. Arthur D Lander, Kimberly K Gokoffski, Frederic Y M Wan, Qing Nie, and Anne L Calof. Cell lineages and the logic of proliferative control. *PLoS biology*, 7(1):e1000015, 2009.

45. Jonathan W Armond, Krishanu Saha, Anas A Rana, Chris J Oates, Rudolf Jaenisch, Mario Nicodemi, and Sach Mukherjee. A stochastic model dissects cell states in biological transition processes. *Scientific reports*, 4(1):3692, 2014.

46. Sameeran Kunche, Huaming Yan, Anne L Calof, John S Lowengrub, and Arthur D Lander. Feedback, lineages and self-organizing morphogenesis. *PLoS computational biology*, 12(3):e1004814, 2016.

47. David A Turner, Penelope C Hayward, Peter Baillie-Johnson, Pau Rué, Rebecca Broome, Fernando Faunes, and Alfonso Martinez Arias. Wnt/β-catenin and fgf signalling direct the specification and maintenance of a neuromesodermal axial progenitor in ensembles of mouse embryonic stem cells. *Development*, 141(22):4243–4253, 2014.

48. Andre Dias, Pau Pascual-Mas, Gabriel Torregrosa-Cortes, Harold M McNamara, Alexandra E Wehmeyer, Sebastian J Arnold, and Alfonso Martinez Arias. A temporal coordination between nodal and wnt signalling governs the emergence of the mammalian body plan. *bioRxiv*, pages 2025–01, 2025.

49. Philip L Townes and Johannes Holtfreter. Directed movements and selective adhesion of embryonic amphibian cells. *Journal of experimental zoology*, 128(1):53–120, 1955.

50. Malcolm S Steinberg and Masatoshi Takeichi. Experimental specification of cell sorting, tissue spreading, and specific spatial patterning by quantitative differences in cadherin expression. *Proceedings of the National Academy of Sciences*, 91(1):206–209, 1994.

51. Ramsey A Foty, Cathie M Pfleger, Gabor Forgacs, and Malcolm S Steinberg. Surface tensions of embryonic tissues predict their mutual envelopment behavior. *Development*, 122(5):1611–1620, 1996.

52. Robert David, Olivia Luu, Erich W Damm, Jason WH Wen, Martina Nagel, and Rudolf Winklbauer. Tissue cohesion and the mechanics of cell rearrangement. *Development*, 141(19):3672–3682, 2014.

53. Tony Y-C Tsai, Mateusz Sikora, Peng Xia, Tugba Colak-Champollion, Holger Knaut, Carl-Philipp Heisenberg, and Sean G Megason. An adhesion code ensures robust pattern formation during tissue morphogenesis. *Science*, 370(6512):113–116, 2020.

54. Guy Pelc, Wesley L McKeithan, Yipei Guo, Michael P Brenner, Wendell A Lim, and Mor Nitzan. Coupling differential adhesion to cell signaling avoids kinetic traps to yield robust multicellular self-organization. *bioRxiv*, pages 2025–10, 2025.

55. Hans-Jörg Fehling, Georges Lacaud, Atsushi Kubo, Marion Kennedy, Scott Robertson, Gordon Keller, and Valerie Kouskoff. Tracking mesoderm induction and its specification to the hemangioblast during embryonic stem cell differentiation. 2003.

56. Nicola Gritti, Jia Le Lim, Kerim Anlaş, Mallica Pandya, Germaine Aalderink, Guillermo Martínez-Ara, and Vikas Trivedi. MOrgAna: accessible quantitative analysis of organoids with machine learning. *Development*, 148(18), 09 2021. dev199611.

57. Sébastien Le Digabel. Algorithm 909: Nomad: Nonlinear optimization with the mads algorithm. *ACM Transactions on Mathematical Software (TOMS)*, 37(4):1–15, 2011.

58. Samuel L Wolock, Romain Lopez, and Allon M Klein. Scrublet: computational identification of cell doublets in single-cell transcriptomic data. *Cell systems*, 8(4):281–291, 2019.

59. F Alexander Wolf, Philipp Angerer, and Fabian J Theis. Scanpy: large-scale single-cell gene expression data analysis. *Genome biology*, 19:1–5, 2018.

60. Paul Van Liedekerke, MM Palm, N Jagiella, and Dirk Drasdo. Simulating tissue mechanics with agent-based models: concepts, perspectives and some novel results. *Computational particle mechanics*, 2(4):401–444, 2015.

61. Brian A Camley and Wouter-Jan Rappel. Physical models of collective cell motility: from cell to tissue. *Journal of physics D: Applied physics*, 50(11):113002, 2017.

62. Alice Gros, Jules Vanaret, Valentin Dunsing-Eichenauer, Agathe Rostan, Philippe Roudot, Pierre-François Lenne, Léo Guignard, and Sham Tlili. A quantitative pipeline for whole-mount deep imaging and multiscale analysis of gastruloids. *bioRxiv*, pages 2024–08, 2024.

S1 Three-state model for cell fate dynamics

Here we use a heuristic approach considering cells transition between different states (*43–46*). We will simplify the branched lineage process obtained using single-cell RNA sequencing analysis in Fig. 2 by combining states 2 and 3 into a single state (B) and states 4, 5 and 6 into a single state (C). Therefore, we will assume unbranched unidirectional transitions between states A (state 1), B and C. Next, we describe the different models discussed in the main text.

Autonomous cell fate dynamics

The simplest possible model is to assume each cell evolves through those states with rates that are unaffected by the presence of other cells. Such a model reads:

$$\dot{\phi}_A = -p\phi_A \tag{S1}$$

$$\dot{\phi}_B = p\phi_A - q\phi_B \tag{S2}$$

$$\dot{\phi}_C = q\phi_B \tag{S3}$$

where ϕ_i is the fraction of cells in state i and $\phi_A + \phi_B + \phi_C = 1$. For the case $p \neq q$, the solution to this linear model reads:

$$\phi_A(t) = \phi_A^0 e^{-pt} \tag{S4}$$

$$\phi_B(t) = (1-\phi_A^0)e^{-qt} + \frac{\phi_A^0 p}{q-p}\left(e^{-pt} - e^{-qt}\right) \tag{S5}$$

where $\phi_A^0 \equiv \phi_A(0)$ and $\phi_C(t) = 1 - \phi_B(t) - \phi_A(t)$. For the particular case $p = q$, the solution takes the form:

$$\phi_A(t) = \phi_A^0 e^{-pt} \tag{S6}$$

$$\phi_B(t) = e^{-pt}\left[1 + \phi_A^0(pt-1)\right] \tag{S7}$$

This extremely simple model can successfully reproduce a maximum in the T+ population over time; however, due to its linear nature, it cannot reproduce the nonlinear dependence on ϕ observed experimentally in Fig. 1D.

Collective cell fate dynamics

Next we consider the case of cell-cell signalling in the cellular aggregate. Let us define the transition rates $\Gamma_{AB}^{(i,\mu)}(\phi_i)$, $\Gamma_{BC}^{(i,\mu)}(\phi_i)$, where μ indicates the type of feedback that applies to the transition ($\mu = +1$, positive; $\mu = 0$, no feedback; $\mu = -1$, negative) and i is the cell population that drives the feedback ($i = A, B$). For simplicity, we will exclude the models where two different cell populations feedback to the same transition (e.g. state A and B, driving a positive feedback on transition AB). A given model is defined by the type of feedback for transitions AB and BC (μ and ν, respectively) and the cell population that controls such feedbacks (i and j, respectively):

$$\dot{\phi}_A = -\Gamma_{AB}^{(i,\mu)}(\phi_i)\phi_A \tag{S8}$$

$$\dot{\phi}_B = \Gamma_{AB}^{(i,\mu)}(\phi_i)\phi_A - \Gamma_{BC}^{(j,\nu)}(\phi_j)\phi_B \tag{S9}$$

$$\dot{\phi}_C = \Gamma_{BC}^{(j,\nu)}(\phi_j)\phi_B \tag{S10}$$

where $\Gamma_{AB}^{(i,\mu)}(\phi_i) = p\Gamma^{(i,\mu)}(\phi_i)$, $\Gamma_{BC}^{(j,\nu)}(\phi_j) = q\Gamma^{(j,\nu)}(\phi_j)$ and Γ is a modulation of the transition rate according to the feedback taking the form:

$$\Gamma^{(i,\mu)}(\phi_i) = \delta_{\mu,0} + \frac{\phi_i\delta_{\mu,1} + K\delta_{\mu,-1}}{K + \phi_i} \tag{S11}$$

where δ_{ij} corresponds to a Kronecker delta. We can rewrite the equations in a dimensionless form by rescaling time by one of the transition rates (we will use q for convenience) such that

we obtain:

$$\dot{\phi}_A = -\alpha\Gamma^{(i,\mu)}(\phi_i)\phi_A \tag{S12}$$

$$\dot{\phi}_B = \alpha\Gamma^{(i,\mu)}(\phi_i)\phi_A - \Gamma^{(j,\nu)}(\phi_j)\phi_B \tag{S13}$$

$$\dot{\phi}_C = \Gamma^{(j,\nu)}(\phi_j)\phi_B \tag{S14}$$

where $\alpha = p/q$ and we have the constraint $\phi_C(t) = 1 - \phi_B(t) - \phi_A(t)$. For the particular case $\mu = -1$, $\nu = -1$ and $i = j = A$, it is possible to solve the dynamics analytically given that the dynamics of A is uncoupled from the dynamics of B and C. The set of equations in this case reads:

$$\begin{aligned} \dot{\phi}_A &= -\frac{\alpha\phi_A}{1+\phi_A/K} \\ \dot{\phi}_B &= \frac{\alpha\phi_A - \phi_B}{1+\phi_A/K} \end{aligned} \tag{S15}$$

and the solution reads:

$$\begin{aligned} \phi_A(t) &= KW\left(\frac{\phi_0}{K}e^{-\alpha t+\phi_0/K}\right) \\ \phi_B(t) &= \frac{1}{1-\alpha}\left[\alpha\phi_A(t) + (1-\phi_0-\alpha)\left(\frac{\phi_A(t)}{\phi_0}\right)^{1/\alpha}\right], \quad \alpha \neq 1, \alpha \neq 0 \\ \phi_B(t) &= (1-\phi_0)\exp\left(-\frac{t}{1+\phi_0/K}\right), \quad \alpha = 0 \\ \phi_B(t) &= \frac{\phi_A(t)}{\phi_0}\left[1-\phi_0+\phi_0\log\left(\frac{\phi_0}{K}\right) - \phi_0\log\left(\frac{\phi_A(t)}{K}\right)\right], \quad \alpha = 1 \end{aligned} \tag{S16}$$

where $\phi_0 \equiv \phi_A(0) = 1 - \phi_B(0)$ and W is the Lambert W function.

S2 Agent-based model details

We next describe the details of the agent-based model used in the main text which combines cell-cell mechanical interactions and the previously described non-autonomous cell fate dynamics. The implementation is done in Julia using the package `CellBasedModels.jl`

Cell Mechanics

We consider the overdamped limit where each cell i at position $\mathbf{x}_i$ follows the dynamics (*60,61*):

$$\lambda_s \mathbf{v}_i + \lambda_r \sum_j (\mathbf{v}_i - \mathbf{v}_j) = \sum_j \mathbf{F}_{ij} \tag{S17}$$

where $\mathbf{v}_i = \dot{\mathbf{x}}_i$, j runs over the nearest neighbours and friction forces on the left-hand side of the equation balance the cell-cell interaction forces on the right-hand side. The parameter λ_s corresponds to an effective cell-ECM friction while λ_r describes the relative cell-cell friction. On the other hand, $\mathbf{F}_{ij}$ corresponds to the cell-cell forces. Eq. S17 can be rewritten as:

$$\Big(\frac{\lambda_s}{\lambda_r n_i} + 1\Big)\mathbf{v}_i = \frac{1}{n_i \lambda_r} \sum_j \mathbf{F}_{ij} + \frac{1}{n_i} \sum_j \mathbf{v}_j \tag{S18}$$

where n_i is the number of nearest neighbours of the $i-$th cell. In our 3D aggregates, we expect cell-cell friction forces to dominate over cell-ECM forces i.e. $\lambda_s \ll \lambda_r$. Using the latter assumption we define a small parameter $\epsilon \equiv \lambda_s/(\lambda_r n_i) \ll 1$ and rewrite force balance as:

$$\mathbf{v}_i = \frac{1}{\lambda n_i} \sum_j \mathbf{F}_{ij} + \frac{1}{n_i} \sum_j \mathbf{v}_j \alpha. \tag{S19}$$

where $\alpha \equiv (\epsilon + 1)^{-1} \lesssim 1$ and $\lambda \equiv \frac{\lambda_r}{\alpha}$ is a friction coefficient. For numerical stability ϵ needs to be non-zero (or equivalently $\alpha < 1$). For simplicity, in our simulations we set α to a constant value slightly smaller than 1.

Cellular forces: $\mathbf{F}_{ij}$ is an effective force that accounts for cell-cell adhesion, volume exclusion and long-ranged cell-cell attractive interactions. The force depends on the position of the two interacting cells (i, j) as well as on their states (s_i, s_j):

$$\mathbf{F}_{ij}(s_i, s_j, d_{ij}) = f(d_{ij})\,\hat{\mathbf{r}}_{ij} \cdot \begin{cases} F_{\text{rep}}^{(s_i,s_j)}, & \text{if } d_{ij} \leq 2r \\ F_{\text{att}}^{(s_i,s_j)}, & \text{if } 2r < d_{ij} < 2\mu r \\ 0, & \text{otherwise} \end{cases} \tag{S20}$$

where s_i, s_j correspond to the state (A, B or C) of the $i-$th and $j-$th cell, respectively; $\hat{\mathbf{r}}_{ij} = \frac{(\mathbf{x}_i - \mathbf{x}_j)}{d_{ij}}$ is the unit vector of the force, $d_{ij} = |\mathbf{x}_i - \mathbf{x}_j|$ is the distance between the two cells and $f(d_{ij}) = \left(\frac{2r}{d_{ij}} - 1\right)\left(\frac{2\mu r}{d_{ij}} - 1\right)$. The parameters $F_{\text{rep}}^{(s_i,s_j)}, F_{\text{att}}^{(s_i,s_j)}$ set the repulsive and attractive force scale and depend on the cellular state (s_i, s_j), thus incorporating homotypic and heterotypic interactions. Finally, the parameter r corresponds to the typical cell radius while the parameter μ is used to set the range of the force.

Cell divisions

Cells divide according to the following rules: 1) A division axis is randomly chosen over the unit sphere. 2) The two daughter cells are generated and positioned on opposite sides of the division axis, centred at the mother cell's location. The centres of mass of the daughter cells are placed at a distance equal to $0.3r$, after which the mother cell is removed. 3) Each daughter cell is assigned a new division time, independently sampled from a uniform distribution with mean τ_{div} and standard deviation σ_{div} (*30*):

$$\text{U}(\tau_{\text{div}}(1 - \sigma_{\text{div}}), \tau_{\text{div}}(1 + \sigma_{\text{div}})) \tag{S21}$$

To prevent artificially large velocities caused by strong repulsive forces immediately after cell division, each daughter cell is assigned a relaxation time τ_{rel}. During this period, we assume that the daughter cells do not contribute to their neighbours' relative friction in Eq. (S17). We

estimate the relaxation time to be roughly inversely proportional to the number of interactions with neighbouring cells. Therefore, we choose that when the cumulative number of interactions reaches a certain value N_{rel}, the daughter cell has relaxed.

Non-dimensional variables and parameters

By non-dimensionalising equation (S19) with respect to a typical distance R_0, force F_0 and timescale T_0, we obtain the equation of motion that is used in the simulations for each cell:

$$\tilde{\mathbf{v}}_i = \frac{1}{\tilde{\lambda} n_i} \sum_j \tilde{\mathbf{F}}_{ij} + \frac{1}{n_i} \sum_j \tilde{\mathbf{v}}_j \alpha \tag{S22}$$

where $\tilde{\lambda} \equiv \lambda R_0/(F_0 T_0)$, $\tilde{v}_i \equiv v_i T_0/R_0$ and $\tilde{F}_{ij} \equiv F_{ij}/F_0$. A similar approach is carried out in order to define all the dimensionless parameters in the simulations, which are denoted by a tilde. $R_0 = 5$ μm is taken as the typical cell radius in gastruloids (*62*), the typical timescale is set as $T_0 = R_0/V_0 = 4$ min, where $V_0 \simeq 1.25$ μm/min is taken as the typical cell instantaneous speed in gastruloids (*26*), and $F_0 = 100$ pN is chosen as the typical cell-cell interaction force.

Polarisation

The degree of polarisation is calculated at every time-step as the normalised distance between the centre of mass of the largest (T+) B-cluster and the centre of mass of the whole aggregate. We use a minimum cluster size of at least 30 cells in order for it to be considered as such and a cutoff distance of $1.5r$. The distance is then normalised by the size of the largest C-cluster in the aggregate. To estimate the size of the largest C-cluster we use the radius of gyration (the root mean square distance of the constituent cells from the cluster centre of mass):

$$R_g = \sqrt{\frac{1}{N} \sum_{i=1}^{N} \left(\mathbf{x}_i - \mathbf{x}_{\mathrm{CM}}\right)^2} \tag{S23}$$

where $\mathbf{x}_i$ are the positions of the cells in the cluster of size N and $\mathbf{x}_{\mathrm{CM}}$ is the position of the cluster's centre of mass.

Supplementary Figures

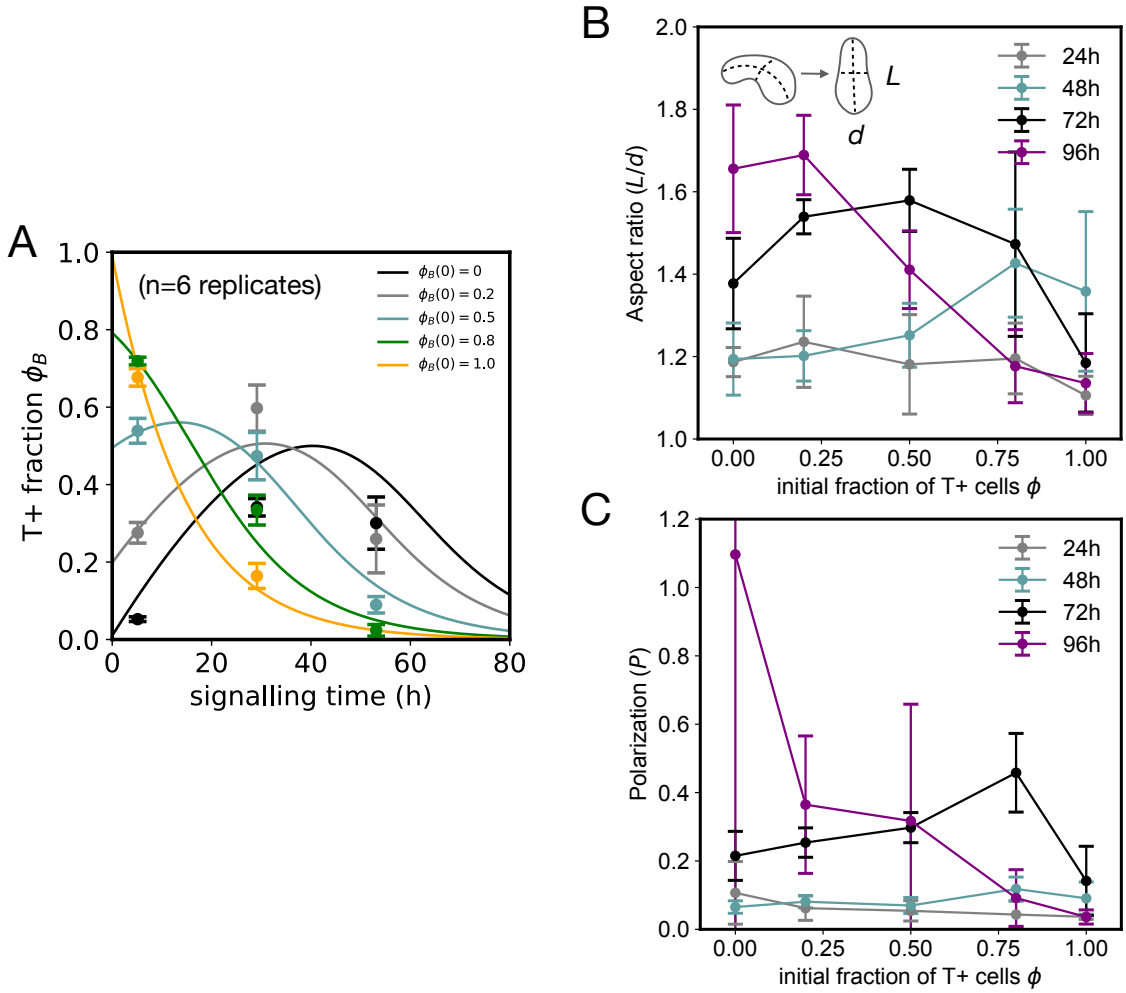

Figure S1: **Initial T+ fraction ϕ_B controls the timing of gastruloid polarisation and elongation**. A) Time evolution of the T+ fraction for different initial conditions. The data is the same as in Fig. 1B,C with the solid lines indicating the corresponding fits to the model. Mean $\pm$ 2 $\times$ SEM. $n = 6$ replicates. B,C) Polarisation and elongation of gastruloids for different initial T+ fractions ϕ. The polarisation P was calculated as the first dipolar moment (see Materials and Methods). Mean $\pm$ SD, $n = 5$ replicates.

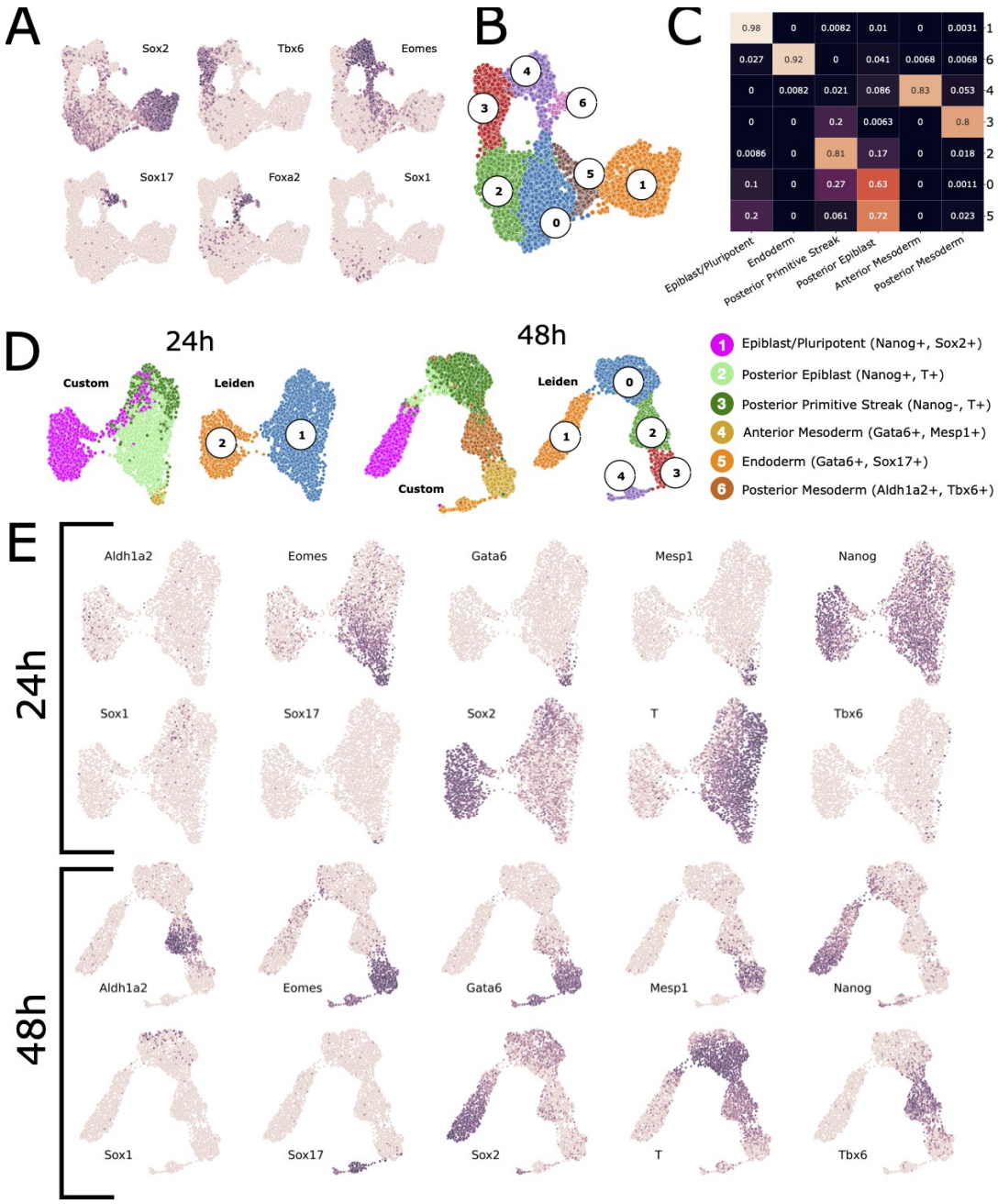

Figure S2: **Additional information of the scRNA-seq dataset presented in the main text**. A) UMAPs integrated analysis (24 hpa and 48 hpa) colored by marker genes used for the annotation of the clusters, in addition to the markers shown in Fig. 2. B) UMAP integrated analysis (24 hpa and 48 hpa) with the identified leiden clusters. C) Confusion matrix normalised by columns showing the consistency of annotation between the annotated clusters in the independent analysis and the integrated analysis cluster annotations. D) UMAPs of the independent analysis at 24 hpa and 48 hpa of the dataset, with the obtained clusters annotated. E) Marker genes expressed over the UMAPs of the time-independent analyses.

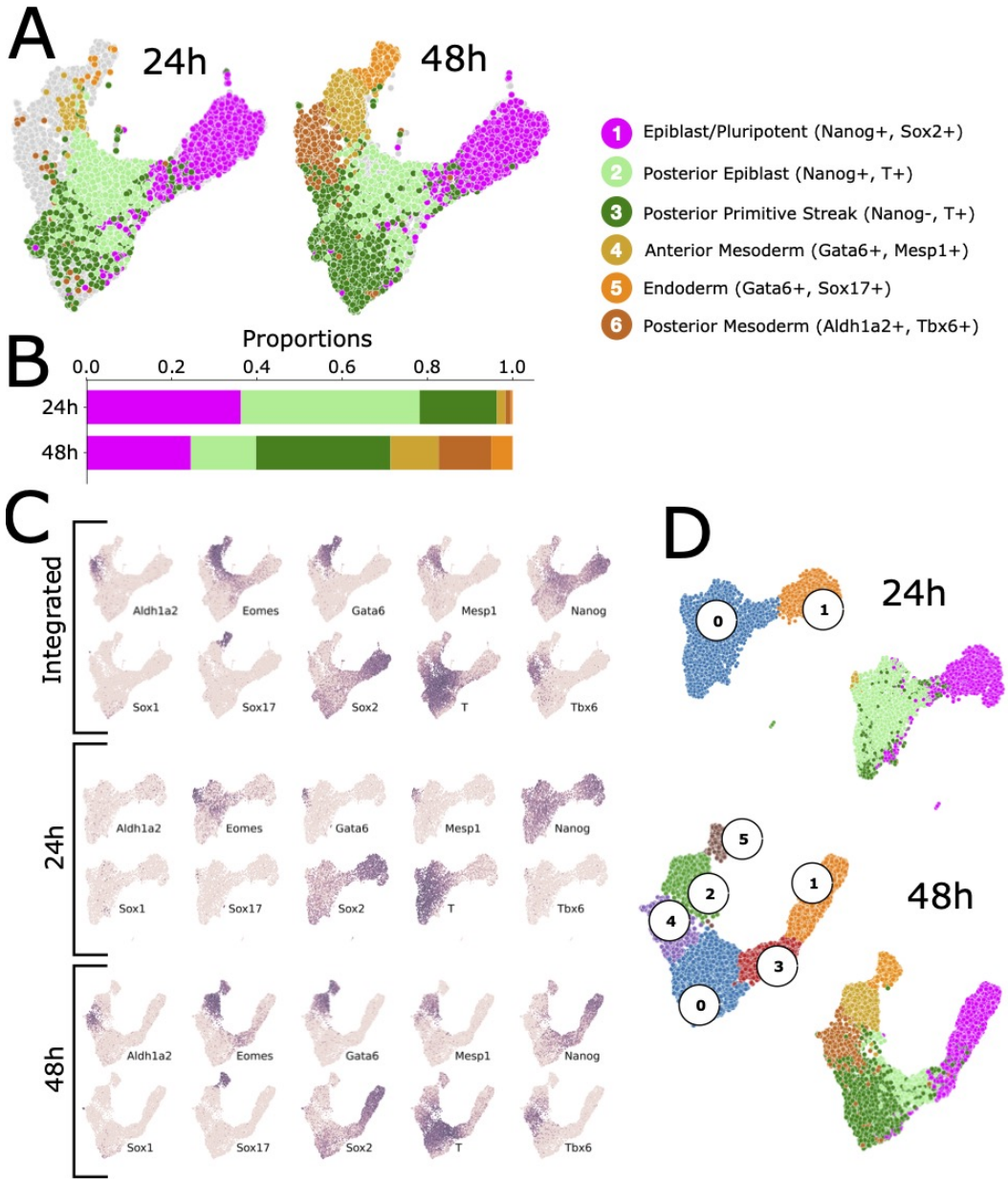

Figure S3: **scRNA-seq analysis of independent gastruloid replicas at 24 hpa and 48 hpa**. A) UMAPs of the integrated analysis of the 24 hpa and 48 hpa datasets with the annotated clusters. B) Proportion of cells per annotation and time point. C) UMAPs of the integrated and independent analysis at 24 hpa and 48 hpa of the dataset, with the marker genes expression color-coded. D) UMAPs of the independent analysis per time-point, showing the leiden clustering and the automatic annotation method.

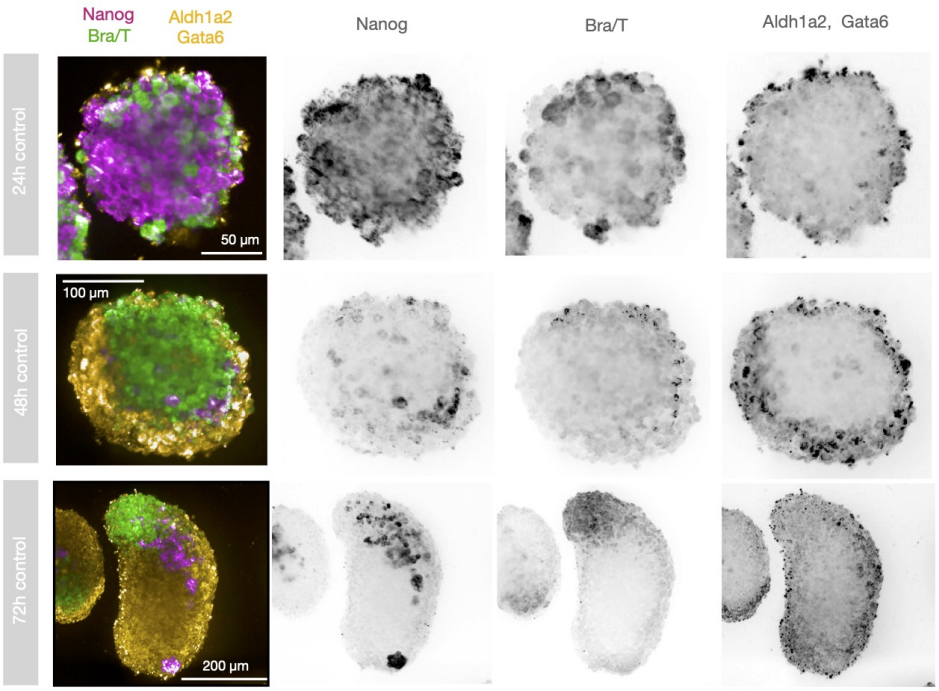

Figure S4: **HCR stainings of gastruloids**. Second replicate as a control. The dynamic range is the same in all images. The images correspond to a maximum intensity projection. T: 488 nm, Nanog: 647 nm, Aldh1a2, Gata6: 546 nm.

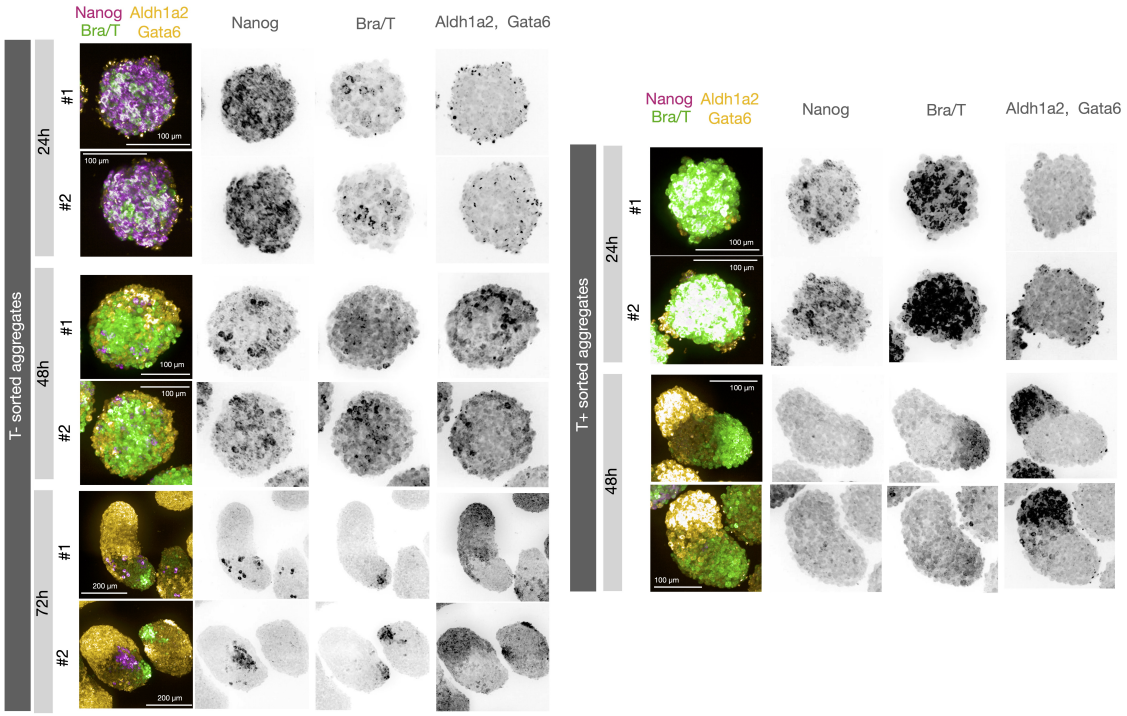

Figure S5: **HCR stainings of T- and T+ aggregates**. The dynamic range is the same in all images and the staining protocol was applied in parallel to the T+ and T- aggregates. The images correspond to a maximum intensity projection. T: 488 nm, Nanog: 647 nm, Aldh1a2, Gata6: 546 nm. No clear signal of the markers could be observed for 72 hpa T+ aggregates.

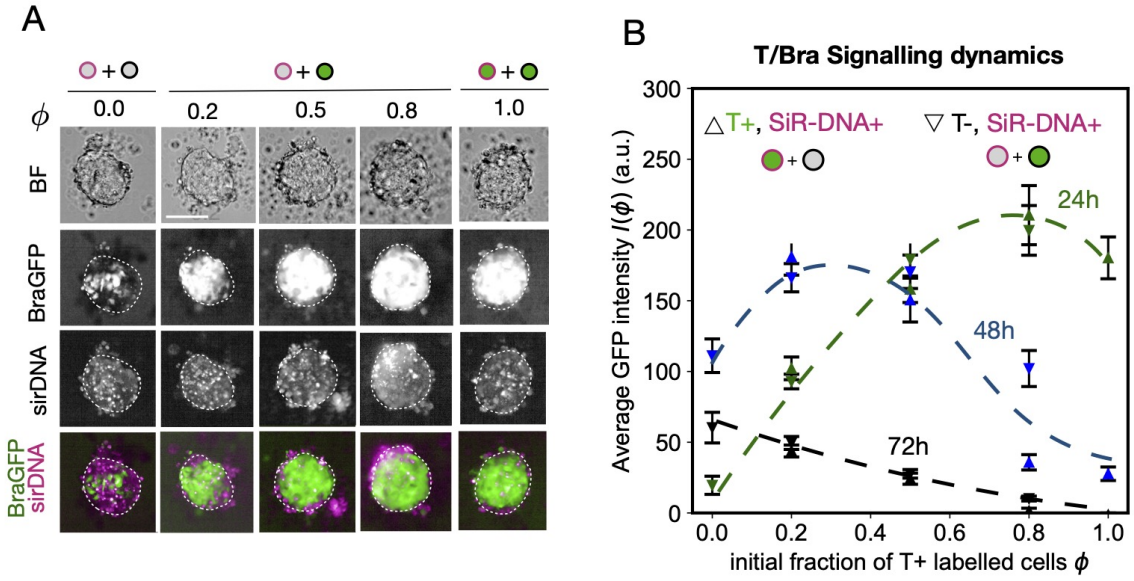

Figure S6: **3D mESC aggregates at 24 hpa for different initial fractions** ϕ. A) Confocal imaging of 3D mES cell aggregates. The panel shows brightfield (BF), T (GFP) and SiR-DNA signals. The images correspond to maximum intensity projections. Scale bar: 100 μm. B) Average GFP intensity $I(\phi)$ versus the initial fraction of T+ labelled cells ϕ adding SiR-DNA to the T+ (upper triangles) or the T- (lower triangles) populations. T dynamics in the aggregates remained unaffected upon the addition of SiR-DNA. Dashed lines are only a guide to the eye. Error bars correspond to SEM.

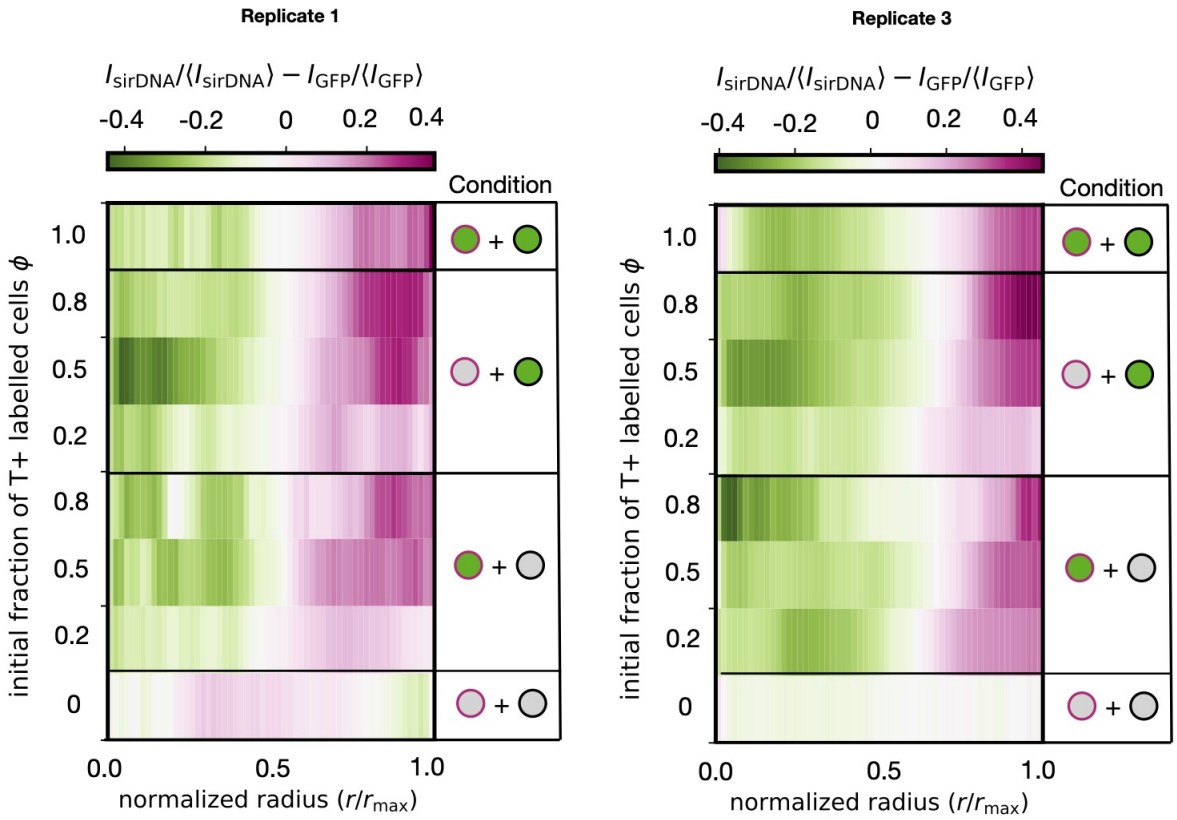

Figure S7: **Radial profiles mESC aggregates**. Colormaps of the radial profile for different starting fractions of T+ (ϕ) and different conditions. Replicates 1 and 3 are shown, while replicate 2 is shown in Fig. 3D. The replicates were done on different days using different batches of cells.

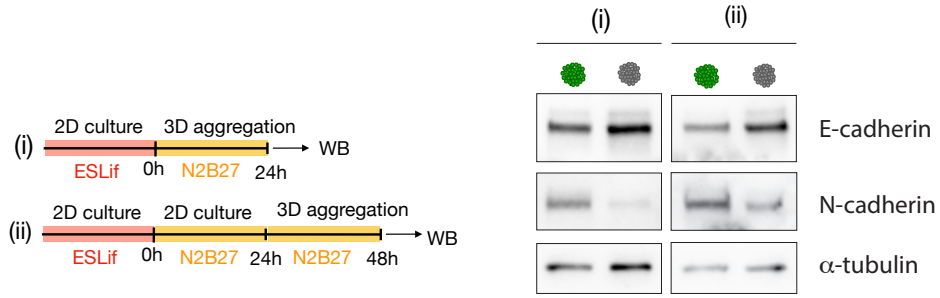

Figure S8: **Cadherin protein levels in T+ and T- aggregates**. FACS sorted T+ and T- aggregates (600 cells) were cultured for 24 hpa (i) or 48 hpa (ii) in N2B27 prior to the lysate. Western blots showed differential protein levels of E and N-cadherin. N- and E-cadherin levels were higher in T+ and T- aggregates, respectively.

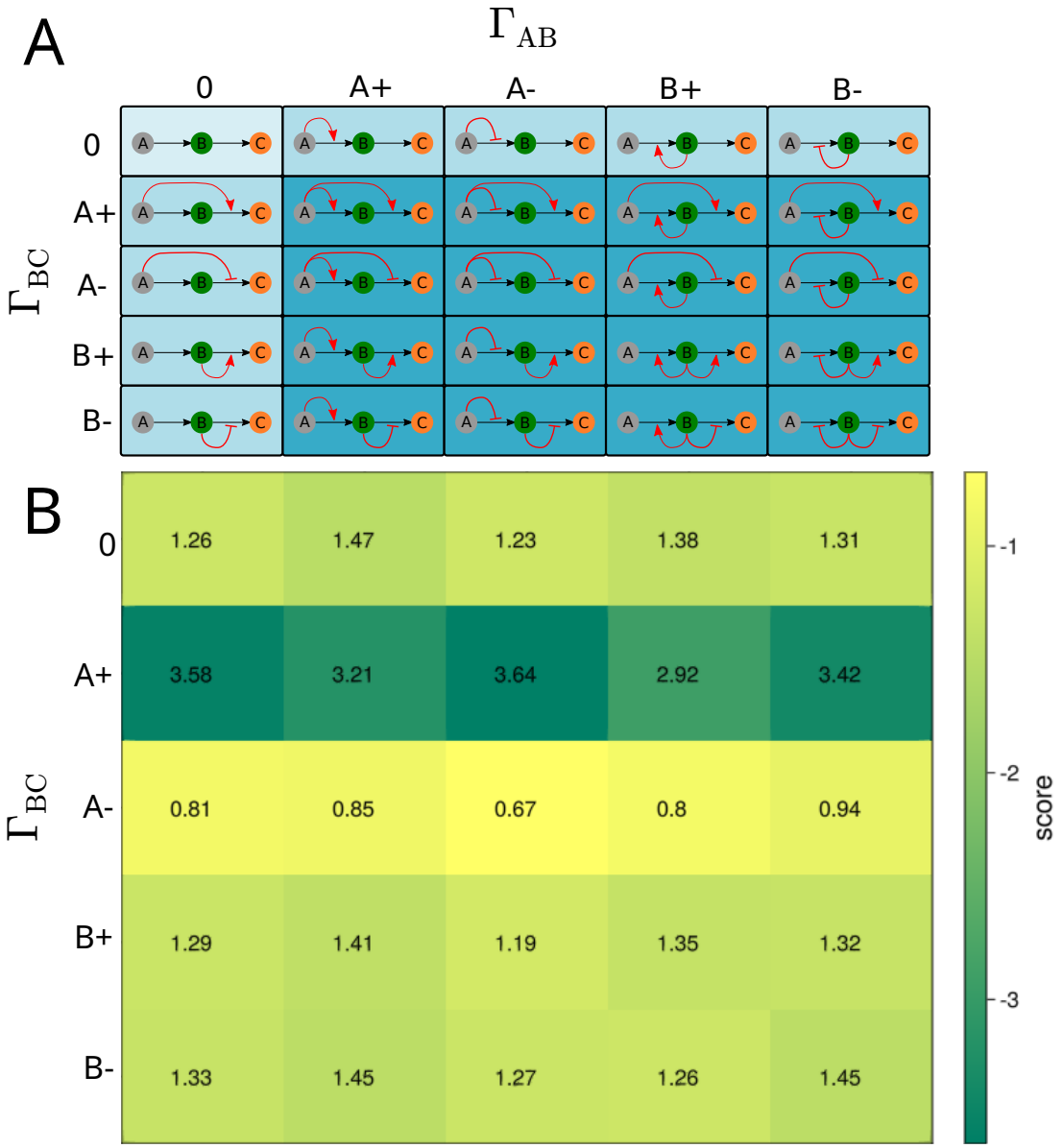

Figure S9: **Cell-cell signalling models**. A) Possible cell-cell signalling models of up to two distinct regulation arrows, on the transition ratios between cell states for the three-state model. B) Loss score of the fit to the data for each of the models described in panel (A). The lower the score, the better the fit to the model. "A+/A-" or "B+/-" indicates that states A or B up-regulate/down-regulate a certain cell fate transition. "0" indicates that a certain cellular state is not regulating a cell fate transition.

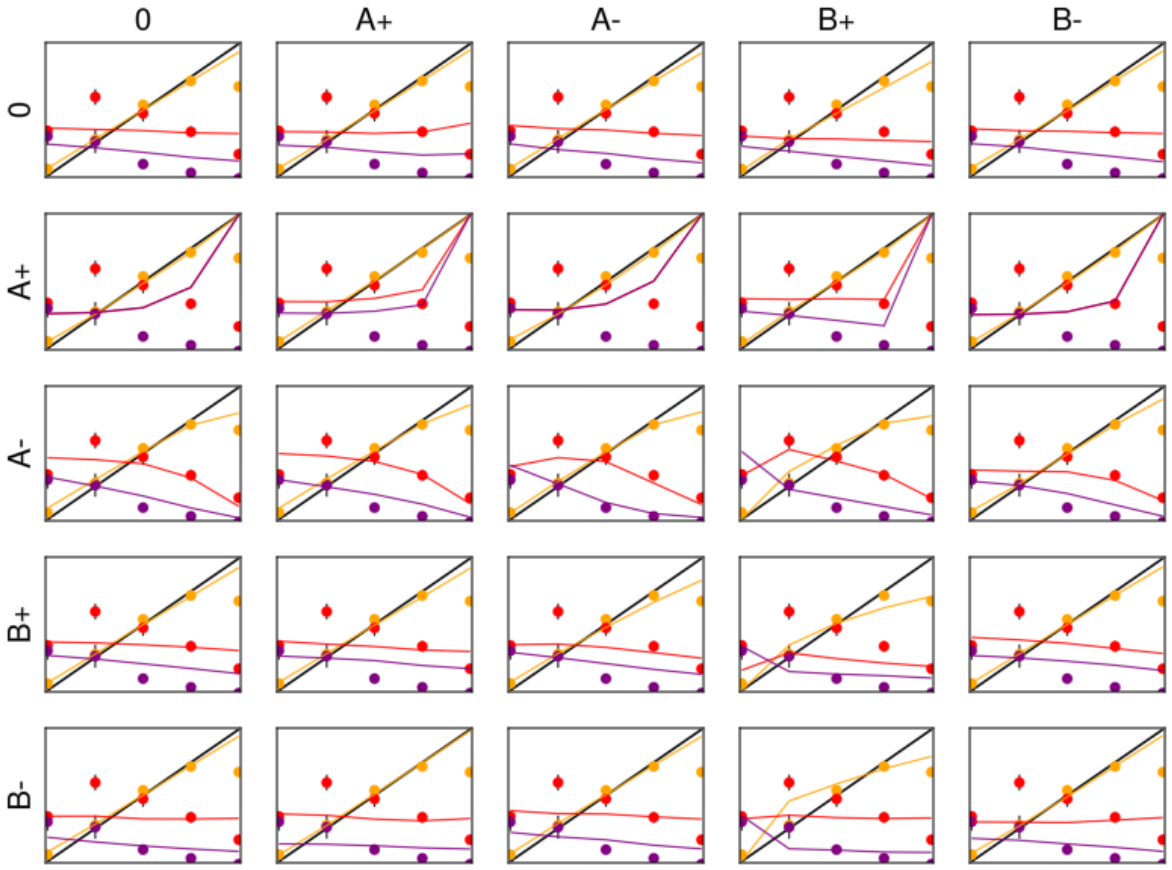

Figure S10: **Best fitting over possible cell-cell communication models**. Solid lines displaying the trends of the best parameter fitting for each model, described in Supplementary Figure S9. Filled circles correspond to the experimental data in Fig. 1D (Yellow: 24 hpa, Red: 48 hpa and Purple: 72 hpa).

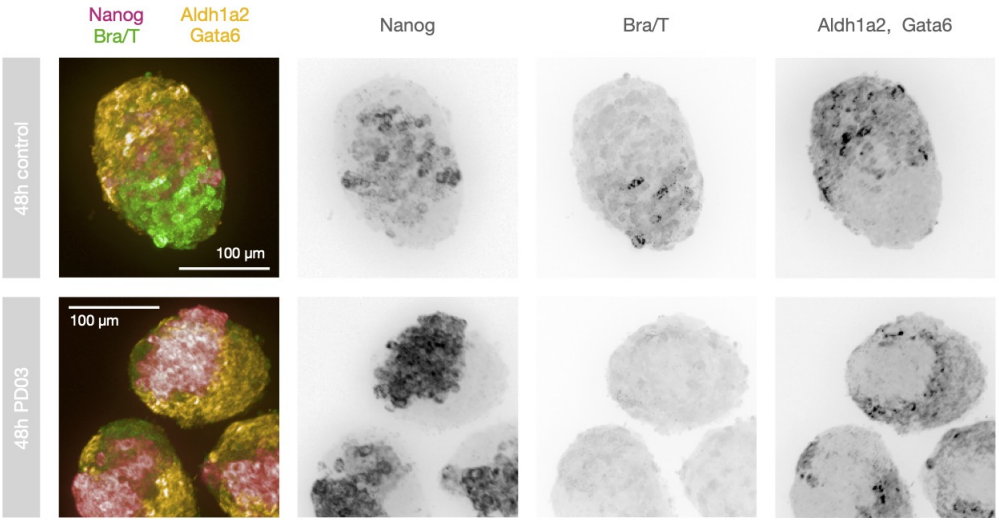

Figure S11: **HCR stainings of 48 hpa cell aggregates for the case $\phi_B(0) = 0.5$ and 1μM PDO3 inhibition from 24 hpa to 48 hpa**. We observe the lack of Bra/T signal in the inhibited aggregates, showing that the A to B transition is halted upon PDO3 treatment. T: 488 nm, Nanog: 647 nm, Aldh1a2, Gata6: 546 nm.

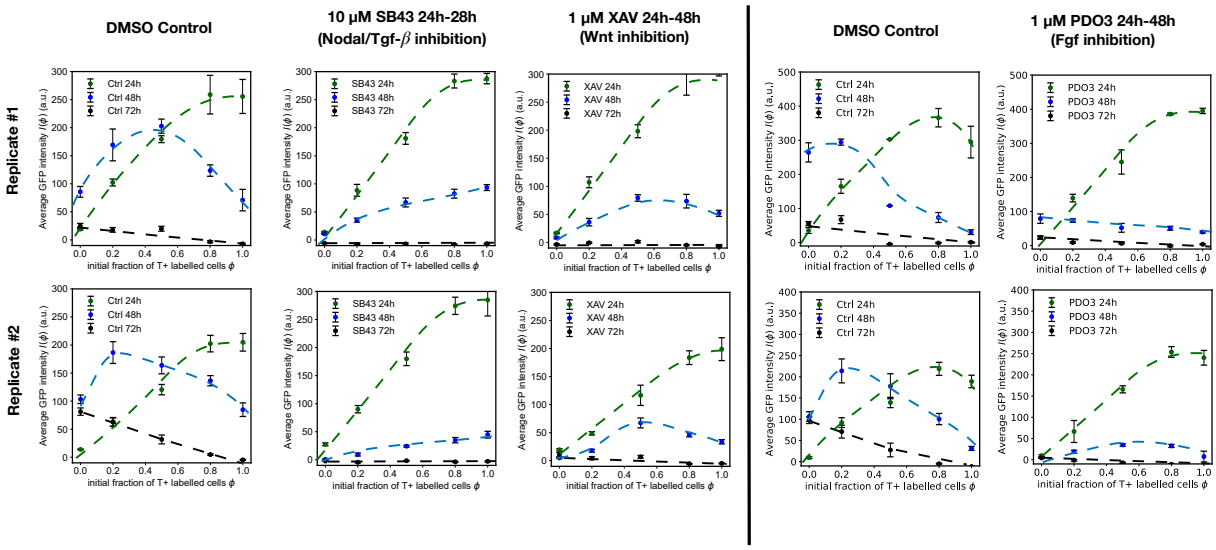

Figure S12: **Effect upon the inhibition of Wnt, Nodal/Tgf-β and Fgf pathways on the evolution of the fraction of cells expressing T at 24, 48 and 72 hpa**. The pathways were inhibited using 1 μM XAV, 10 μM SB43 and 1 μM PDO3, respectively. The different inhibitors were incubated from 24 to 48 hpa. Mean $\pm$ SEM. The replicates for Fgf inhibitions were conducted on different days than the Wnt and Nodal/Tgf-β inhibitions. Dashed lines are only a guide to the eye.

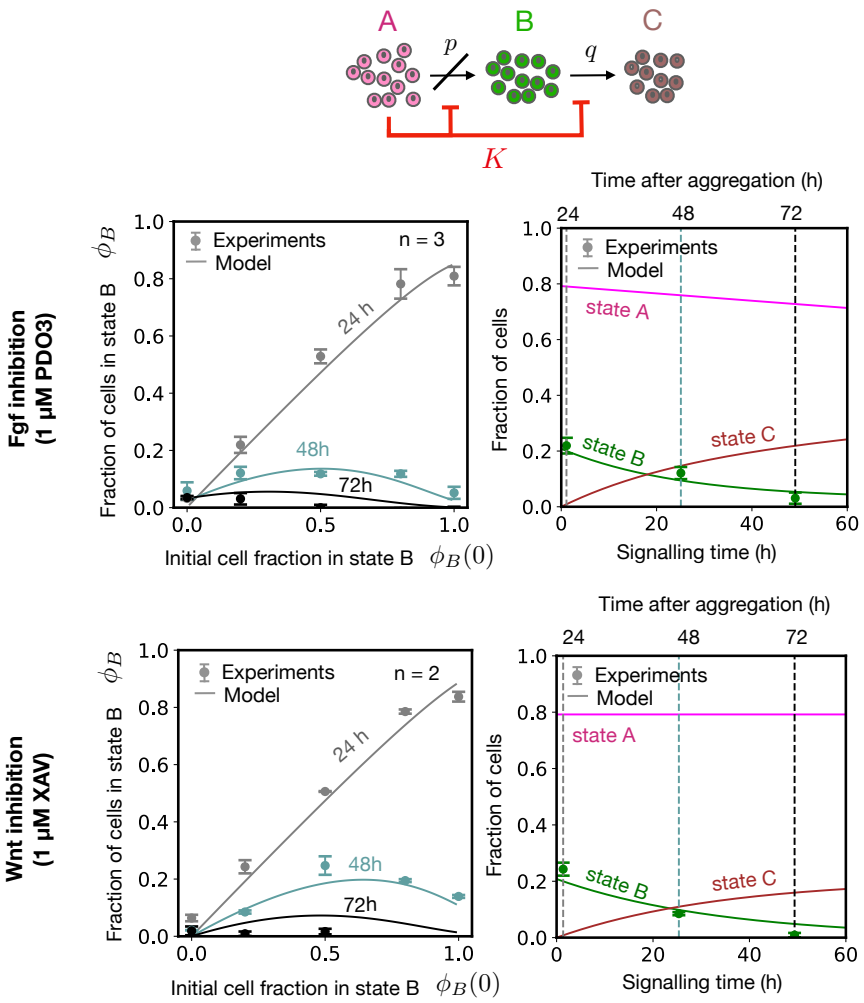

Figure S13: **Effect upon the inhibition of Wnt and Fgf pathways on the evolution of the fraction of cells expressing T at 24, 48 and 72 hpa**. (Left) Cell proportion plots as a function of time. (Right) Fractions of cells A, B and C as a function of time. For both cases, solid lines correspond to fits to the model. The Wnt pathway was inhibited with 1 μM XAV and the Fgf pathway was inhibited with 1 μM PDO3. Both inhibitors were incubated from 24 to 48 hpa. Error bars correspond to 2 $\times$ SEM over different replicates. For the case of Wnt inhibition, the fit with $p = 0$ is shown; however, for the case of Fgf inhibition, the best fit for small non-zero p is shown (see Table S3)

Annotation	Genes
Epiblast/Pluripotency	Nanog+, Sox2+
Posterior Epiblast	Nanog+, T+
Posterior Primitive Streak	Nanog-, T+
Anterior Mesoderm	Eomes+, Gata6+, Mesp1+
Posterior Mesoderm	Aldh1a2+, Tbx6+
Endoderm	Eomes+, Gata6+, Sox17+

Table S1: **Annotation markers**.

Antibody	Company	Catalogue number	Dilution
anti-E-Cadherin	Cell Signaling	3195	1:2000
anti-N-cadherin	Abcam	ab18203	1:2000
anti-α-catenin	Merck (Sigma)	T6199	1:1000

Table S2: **Primary antibodies used for the Western Blots**.

Condition	n	$p\ (h^{-1})$	$q\ (h^{-1})$	K	$T_{24}\ (h)$
Control	4	0.14 ± 0.01	0.071 ± 0.003	0.17 ± 0.02	5.1 ± 0.5
PDO3	4	0.006 ± 0.001	0.15 ± 0.01	0.30 ± 0.04	1.09 ± 0.06
	3	0 (fixed)	0.4 ± 0.1	0.10 ± 0.07	0.6 ± 0.1
XAV	4	$(8.8 \pm 0.2) \cdot 10^{-5}$	0.088 ± 0.002	0.40 ± 0.03	1.36 ± 0.03
	3	0 (fixed)	0.088 ± 0.002	0.40 ± 0.03	1.4 ± 0.1
SB43	4	$(7.2 \pm 0.1) \cdot 10^{-5}$	0.072 ± 0.001	1.7 ± 0.2	1.6 ± 0.1
	2	0 (fixed)	0.0660 ± 0.0004	∞ (fixed)	1.5 ± 0.1

Table S3: **Fitted model parameters in the different conditions.** The value n indicates the number of fitted parameters.

Table S4: Main agent-based model parameters. *: Orientative cell-division timescales estimated from Ref. (*36*). †: Experimentally obtained parameters in this work.

Parameter	Symbol	Value
Time step	$\tilde{\Delta t}$	0.02
Characteristic length	$\tilde{r}$	1
Force range parameter	μ	2
Average cell division time for state A	$\tilde{\tau}_{\mathrm{div},A}$	$300^\star$
Average cell division time for state B	$\tilde{\tau}_{\mathrm{div},B}$	$300^\star$
Average cell division time for state C	$\tilde{\tau}_{\mathrm{div},C}$	$750^\star$
SD of cell division time	$\tilde{\sigma}_{\mathrm{div}}$	0.5
Effective friction coefficient	$\tilde{\lambda}$	1
Cell-ECM/cell-cell friction parameter	α	0.9
$A \to B$ transition rate	$\tilde{p}$	$0.009333^\dagger$
$B \to C$ transition rate	$\tilde{q}$	$0.004667^\dagger$
Cell division relaxation time	N_{rel}	150
Feedback parameter	K	$0.2^\dagger$

Table S5: Homotypic and heterotypic interaction parameters.

Parameter	Value
Attraction force AA, BB, AB $\tilde{F}_{\mathrm{att}}^{(A,A)}, \tilde{F}_{\mathrm{att}}^{(B,B)}, \tilde{F}_{\mathrm{att}}^{(A,B)}$	6.0
Attraction force CC $\tilde{F}_{\mathrm{att}}^{(C,C)}$	4.8
Attraction force AC $\tilde{F}_{\mathrm{att}}^{(A,C)}$	2.4
Attraction force BC $\tilde{F}_{\mathrm{att}}^{(B,C)}$	1.6
Repulsion force CC $\tilde{F}_{\mathrm{rep}}^{(C,C)}$	5.1
Repulsion forces (other) $\tilde{F}_{\mathrm{rep}}^{(A,A)}, \tilde{F}_{\mathrm{rep}}^{(B,B)}, \tilde{F}_{\mathrm{rep}}^{(A,B)}, \tilde{F}_{\mathrm{rep}}^{(B,C)}, \tilde{F}_{\mathrm{rep}}^{(A,C)}$	3.0